Behaviour of reinforced ultra-high performance concrete slabs under impact loading after exposure to elevated temperatures

Kaiyi Chi[1], Jun Li[1*], Chengqing Wu[1*]

[1]School of Civil and Environmental Engineering, University of Technology Sydney, NSW 2007, Australia

Abstract

Steel fibre reinforced ultra-high performance concrete (UHPC) material is prone to spalling under elevated temperatures. However, with addition of polypropylene (PP) fibre, thermal spalling of UHPC can be mitigated and its fire resistance can be improved. This research investigates the impact resistance of steel and PP fibre reinforced UHPC slabs after exposure to elevated temperatures, and the structural behaviour and damage were compared with normal strength concrete (NSC) slabs. Karagozian & Case concrete (KCC) model was adopted to simulate both NSC and UHPC materials. With consideration of thermal hazards, the material damage, equation of state and strain rate sensitivity were adapted. The validity of this numerical model was evaluated against available experimental results. After being exposed to fire hazards, the numerical model was subsequently used to forecast the impact resistance of the reinforced UHPC slabs. The effect of fire exposure time, impact velocity and impact mass on the resistance of the reinforced NSC and UHPC slabs were analysed. The simulation results revealed that punching shear failure areas in the NSC slabs were 2.5 times, 3.4 times, 3.0 times and 1.2 times larger than the UHPC slabs after exposure to international standardization ISO-834 standard fire for 1, 2, 3 and 4 hrs, respectively. After exposure to the standard fire ISO-834 for 2 hrs, the punching shear failure on the bottom side of NSC increased 90.9% with the increase in falling height from 1 m to 7 m, while for the UHPC slabs, the increment was around 67.9%. After exposure to the standard fire ISO-834 for 2 hrs, the punching shear damage of the NSC slabs was increased by 72.9% with the punch weight increased from 100 kg to 700 kg, whereas the damage in the UHPC slabs was increased by 53.8%.

Keywords: ultra-high performance concrete, impact load, high temperature, KCC model, numerical investigation;

1 Introduction

Nowadays, reinforced concrete structures are experiencing ever-growing threats from natural and man-made hazards. A growing amount of focus is being placed on the safety of concrete components regarding extreme loads such as fire, impact and blast. Fire accidents occur frequently, which are commonly accompanied by blast and/or impact effect, resulting in significant harm to reinforced concrete structures. Concrete and its structures were found to experience brittle failure under impulsive loads, and extensive thermal spalling and strength degradation under elevated temperatures. To date, failure mechanism of concrete material and components under single type of hazard such as high temperature or dynamic loads has been extensively investigated [1-4], but their responses subjected to combined hazards are rarely analysed.

*Corresponding author at: School of Civil and Environmental Engineering, University of Technology Sydney, Sydney, NSW 2007, Australia.
E-mail address: Jun.Li-2@uts.edu.au (J. Li), Chengqing.Wu@uts.edu.au (C. Wu)

Normal strength concrete (NSC) has a low tensile performance, quasi-brittle, and is vulnerable to brittle shear damage from impulsive loads [5-7]. The mechanical and physical behaviour of NSC is also known to be signally affected by the high temperature [2, 8, 9]. The destruction of calcium silicate hydrate (C-S-H) molecular structure influences the compressive and residual strengths of the concrete above 500 ℃ [10]. Concrete may lose its strength completely at 1000 ℃ temperature owing to dehydration of calcium hydroxide ($Ca(OH)_2$) and decomposition of calcium carbonate ($CaCO_3$). Concrete modulus of elasticity also undergoes distinct degradation under/after high temperature (up to 84.6% at 800 ℃), which significantly affects deformation capability of concrete structures under/after exposure to fire.

Emerging as a new construction material, ultra-high performance concrete (UHPC) exhibits high mechanical strength and material ductility [6]. Many experiments and numerical simulations have focused on the behaviour of UHPC components against dynamic loads (impact loads or blast loads) [6, 11-13]. The reinforced UHPC columns under lateral impact stresses were the subject of the experimental and numerical research by Wei et al. [14]. The reinforced UHPC columns were revealed to exhibit a high impact resistance. Yoo and Banthia [13] investigated the ultra-high-performance fibre-reinforced concrete (UHPFRC) components, including beams, slabs and columns with different fibre content and aggregates with respect to impact and blast resistance. It was noted that UHPFRC had a higher impact resistance than traditional concrete, and the impact resistance of UHPFRC was relevant to fibre orientation. Wang et al. [15] tested UHPFRC subjected to lateral impact loading. It indicated that the UHPFRC filled steel tubular members demonstrated a higher resistance than NSC counterparts, which included less deflection, less indentation and higher stiffness.

When fire accidents occur, UHPC is susceptible to explosive spall ascribed to its low porosity [16]. Many researches have been devoted to the mechanical behaviour of UHPC under and after elevated temperature [17-20]. The results demonstrated that the compressive strength (both the residual and "hot state" strength) of UHPC would first increase (up to 200 °C due to the promotion of the hydration) and then decrease when the temperature further elevates. The residual compressive strength after exposure to 800 °C was roughly 20% of that at room temperature [18]. To enhance the thermal resistance of UHPC and reduce the thermal spalling, many scholars have adopted synthetic fibres with low-melting point such as polypropylene (PP) [21], polyvinyl alcohol (PVA) [22] to the manufacturing of UHPC. Felicetti [21] reported that the loss of tensile strength was approximately 55% in the UHPC which contained 2% steel fibre and 2% PP after exposure to 500 °C. Sanchayan and Foster [22] developed UHPC with hybrid steel and PVA fibre, which can remain 50% of its original residual compressive strength between 500 °C and 600 °C. Zhang et al. [23] added natural jute fibre which shrinks with elevated temperature in UHPC. It demonstrated that the UHPC residual compressive strength with 10 kg/m^3 jute fibres retained 43.6% of its origin strength after exposure to 800 °C.

A few studies were performed on NSC under combined thermal and dynamic loadings to effectively evaluate the mechanical characteristics of concrete affected by elevated temperature [24-27]. Huo et al. [28] employed a split Hopkinson pressure bar (SHPB) test to analyse the dynamic behaviour of NSC after exposure up to 700 °C. It indicated that NSC rate sensitivity was dramatically affected by high temperature. The impact of high temperature on the dynamic increase factor (DIF) diminished as the temperature increased. Zhai et al. [29] performed SHPB tests to explore NSC after exposure up to 1000 °C with strain rate varying from 10^{-4} to 300 s^{-1}. The results demonstrated DIF decreased from 600 °C and 800 °C, whereas increased between 800 °C and 1000 °C. However, only a few researchers have focused on the dynamic behaviour of UHPC after exposure to fire. The SHPB tests for UHPC after heated to temperature up to 800 °C were conducted by Liang et al. [30]. It was revealed that the strain rate increased dramatically from room temperature to 200 °C but visually declined between 200 °C to 600 °C, and it also increased between 600 °C and 800 °C.

Until now, limited tests have been conducted on concrete structures against combined fire and dynamic loads. Jin et al. [31] analysed the response of the RC slabs under impact performance and compared the failure patterns, mid-span deflection, impact force, dissipation of impact energy at/after high temperature via numerical simulation. They demonstrated that the stiffness of the RC slab decreased and the energy dissipation increased as the fire duration prolonged. Ožbolt et al. [32] also explored the impact resistance of the RC slabs after fire via finite element (FE) model combined with thermo-mechanical method. The findings revealed that the impact resistance of the RC slabs remarkably decreased after exposing to fire. Jin et al. [33] analysed the behaviour of the RC beams against high temperature and impact loadings by FE model. They found out that the RC beams experienced more severe damage under the thermal state than after cooling down. Ožbolt et al.[34] examined the dynamic behaviour of the RC frames after thermal pre-damage by both physical experiment and numerical simulation. It demonstrated the superior impact resistance of the RC frame after cooling down than under the high temperature exposure due to the recovery of reinforcement. Ruta et al. [35] reported a experimental test with respect to thermo-impact combined load on the RC slabs, which was set up in Bhabha Atomic Research Centre (BARC), Mumbai, India. The standard fire ISO-834 was used to heat the RC slabs for 1 hr and 25 thermocouples were installed in the RC slabs. After heating for 60 minutes, the RC slabs were cooled down prior to the impact test. A 588 kg hammer was placed in 5 m height to drop down. Some of the experimental data has been recorded such as temperature-time curve at different thickness depths, impact load and strain-time history of the RC slab. In regards to UHPC structures under combined hazards, a close-range field blast test was conducted by Chen et al. [36] on the reactive power concrete-filled steel tubular (RPC-FST) columns after exposure to fire. It was revealed that the RPC-FST columns retained good blast resistance after exposure to fire. Furthermore, the deformation types transitioned from elastic to plastic as the fire duration increased.

In the present study, a UHPC reinforced by hybrid steel fibre and PP fibre (Xu et al. [37]) was utilised to explore the impact resistance of the UHPC slabs after exposure to high temperature. According to a previous experimental investigation, 58% of its initial compressive strength of this UHPC material could still be retained after exposure to 800°C. A refined numerical model was established to explore the post-fire impact resistance of both the NSC and UHPC slabs. Extensive modification on the material constitutive model was performed to take the thermal effects into consideration. The impact response of the NSC and UHPC slabs were compared with consideration of varying fire damage and impact scenarios.

2 Constitutive models and material properties

2.1 KCC Concrete model

Many concrete constitutive models such as Karagozian & Case Concrete model (KCC) [38], Riedel-Hiermaier-Thoma (RHT) model [39] and the Continuous Surface Cap Model (CSCM) are available in commercial software LS-DYNA [40] and are extensively used on NSC structural modelling against impact/blast loads. For normal strength concrete (NSC), the KCC model parameters can be derived automatically using uniaxial compressive strength. This feature renders KCC a very popular concrete constitutive model especially when material characterizing results are not available. However, to better simulate the behaviour of UHPC, it is required to adjust the parameters of the KCC model due to the varied mechanical properties, particularly the tensile capability of UHPC [41]. The fire induced strength/stiffness degradation, rate sensitivity change and damage also need to be considered for both NSC and UHPC prior to performing the multi-hazard (fire and impact load) analysis in the KCC model.

2.1.1 Strength surface parameters

The initial yield strength surface $\Delta\sigma_y$, maximum strength surface $\Delta\sigma_m$, and residual strength surface $\Delta\sigma_r$ are the three independent strength surfaces defined by the KCC model [38]. The following definitions apply to these three shear strength surfaces,

$$\Delta\sigma_m = a_0 + \frac{p}{a_1 + a_2 p} \quad \text{(maximum strength surface)} \tag{1}$$

$$\Delta\sigma_r = \frac{p}{a_{1f} + a_{2f} p} \quad \text{(residual strength surface)} \tag{2}$$

$$\Delta\sigma_y = a_{0y} + \frac{p}{a_{1y} + a_{2y} p} \quad \text{(yield strength surface)} \tag{3}$$

where

$$\mathrm{p} = -\frac{\sigma_1 + \sigma_2 + \sigma_3}{3} \tag{4}$$

is the hydrostatic pressure with σ_1, σ_2 and σ_3 being the principal stresses. Seven material strength surface parameters are $a_0, a_1, a_2, a_{1f}, a_{2f}, a_{1y}, a_{2y}$. Joy and Moxley [42] demonstrated that the initial yield strength for NSC is 0.45 times of its maximum strength under triaxial compression. The equivalent yield surface point (p', σ_y) can be empirically estimated using Eq. (5) according to the maximal strength surface point (p, σ_m). The maximum and residual strength can be determined by using the triaxial stress-strain curve. It is worth noting that because the residual strength is zero under unconfined compression test, the residual strength will be zero when the pressure is equal to zero.

$$\begin{cases} \Delta\sigma_y = 0.45\ \Delta\sigma_m \\ \mathrm{p'} = \mathrm{p} - \dfrac{0.55}{3}\Delta\sigma_m \end{cases} \tag{5}$$

Using linear interpolation method, the current failure surface of concrete under different states can be determined with the consideration of the accumulated damage as follows,

$$\Delta\sigma = \sqrt{3J_2} = \begin{cases} \Delta\sigma_y + \eta(\Delta\sigma_m - \Delta\sigma_y), & \lambda \le \lambda_m \quad \text{Strain hardening} \\ \Delta\sigma_r + \eta(\Delta\sigma_m - \Delta\sigma_r), & \lambda > \lambda_m \quad \text{Strain softening} \end{cases} \tag{6}$$

where $J_2 = \frac{(\sigma_1 - \sigma_2)^2 + (\sigma_2 - \sigma_3)^2 + (\sigma_1 - \sigma_3)^2}{6}$ is the second deviatoric stress invariant, η presents the scale factor which is related to the modified effective plastic strain λ. $\eta(\lambda)$ value varies from 0 to 1. The value of η is determined by the damage variable λ. It indicated stain hardening phase where λ increases from 0 to λ_m, and η increases from 0 to 1. It represents for strain softening when η decreases from 1 to 0.

Triaxial compression tests with various confinement levels and unconfined compression tests can also yield data on the strength meridian. Using the unconfined compressive strength of concrete, the KCC model is automatically produced. The following scaling law can be used to create the compressive strength surface characteristics for an updated concrete model in which unconfined compressive strength is given.

$$a_{0n} = a_0 r,\ a_{1n} = a_1,\ a_{2n} = a_2 r \tag{7}$$

where $r = \frac{f_{c,new}}{f_{c,old}}$, the unconfined compressive strength of a previously modelled concrete is represented by $f_{c,old}$. The following Eqs. (8)-(10) are used to determine the strength surface parameters of a generic concrete [43].

$$a_0 = 0.2956\ f_c;\ a_1 = 0.4463;\ a_2 = 0.0808/\ f_c \tag{8}$$

$$a_{0y}=0.2232\, f_c;\ a_{1y}=0.625;\ a_{2y}=0.2575/\, f_c \quad (9)$$

$$a_{0f}=0;\ a_{1f}=0.4417;\ a_{2f}=0.1183/\, f_c \quad (10)$$

In the present study, uniaxial compressive strength with 45 MPa for NSC [44] and uniaxial compressive strength with 129 MPa for UHPC are used as examples [45]. The corresponding strength surface parameters are displayed in Table 1.

Table 1

Parameters for strength surfaces in KCC model.

	a_0	a_1	a_2	a_{1f}	a_{2f}	a_{0y}	a_{1y}	a_{2y}
Original KCC 45.4 MPa	1.34E+07	0.4463	1.78E-09	0.4417	2.61E-09	1.01E+07	0.625	5.67E-09
NSC 45 MPa KCC default	1.33E+07	0.4463	1.8E-09	0.4417	2.63E-09	1.00E+07	0.625	5.72E-09
UHPC 129 MPa (⌀50*100 mm) **[45]** default	3.81E+07	0.4463	6.26E-10	0.4417	9.17E-10	2.88E+07	0.625	2.00E-09
UHPC 129 MPa **[45]**modified	4.76E+07	0.4789	7.35E-10	0.4417	9.17E-10	2.88E+07	0.435	2.00E-09

Figures 1 (a)&(b) show the triaxial compression test results for both NSC and UHPC, respectively. In terms of NSC, it is evident that the results of the triaxial compression test basically agree well with the KCC predicted curve at ambient temperature. However, for UHPC, the automatically generated strength surfaces do not fit well with the test results when the hydrostatic pressure increases from Figure 1(b). The strength surface of UHPC should be altered to emulate the triaxial properties of the algorithm more accurately. Previous trials by Xu et al. [46] have proved that the triaxial test data are consistent with the modified strength surfaces after modifying a_0, a_1, a_2, a_{1y} that are listed in Table 1.

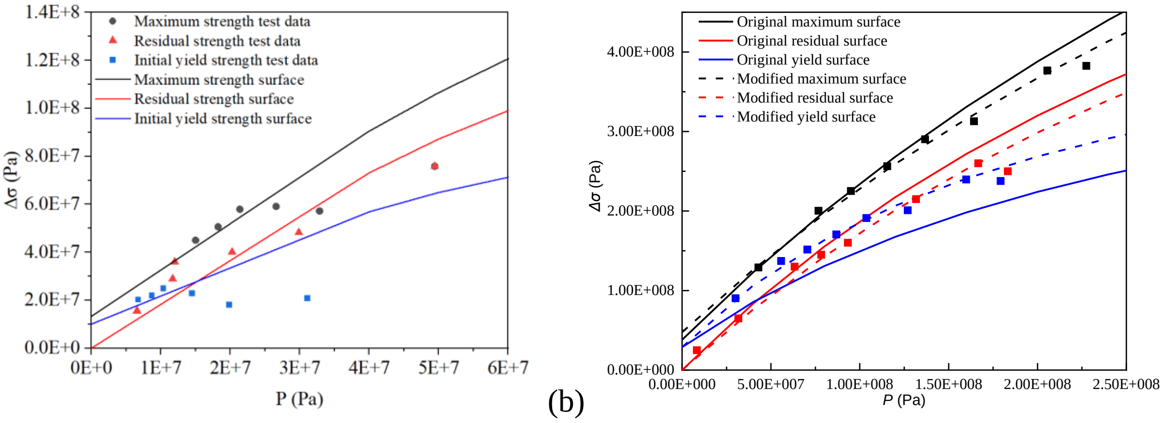

(a) (b)

Figure 1. Triaxial compression behaviour of 45 MPa NSC and 129 MPa UHPC under ambient temperature [46].

At high temperature, the change in compressive strength for concrete is attributed to the physical properties such as heat conductivity and thermal expansion as well as chemical characteristics such as thermal stability [47]. When heated to 80 to 100 ℃, the evaporated water reduces the van der Waals force between C-S-H layer, and concrete loses its compressive strength with an increase in temperature. Calcium hydroxide $Ca(OH)_2$ decomposes into calcium oxide and water above 400 ℃ [48]. While above 500 ℃, the compressive and residual strengths of concrete are visibly reduced ascribed to the destruction of C-S-H molecular structure [10]. In the present study, the modification of the shear strength surface of NSC after high temperature is based on the triaxial compression tests from Hammoud et al. [44] and values of the triaxial compressive strength at various confining pressures with different target temperatures are summarised in Table 2. All specimens were cooled down to room temperature before testing.

Table 2
Results of triaxial compression test on NSC cylindrical specimens [44].

Temperatures T(ºC)	Uniaxial compressive strength $f_{c,T}$(MPa)	Confining pressure σ_3 (MPa)	Triaxial compressive strength σ_1^u (MPa)
25	45	0	45.0
		1.38	52.0
		2.07	60.0
		6.89	66.0
		13.79	71.0
		24.1	100.0
300	30	0	30.0
		1.38	37.0
		2.07	37.0
		6.89	59.0
		13.79	80.0
		24.1	111.0
500	17	0	17.0
		1.38	27.0
		2.07	31.0
		6.89	57.0
		13.79	79.9
		24.1	110.0
700	9	0	9.0
		1.38	20.0
		2.07	23.0
		13.79	68.0
		24.1	81.9

By altering the settings of the three shear strength surfaces in the KCC model, it is possible to determine the performance of NSC after exposure to various increased temperatures using the data provided above, shown in Table 3. a_1, a_{1f} and a_{1y} remain unaltered while the other strength surface parameters are adjusted acquired from the triaxial test results. It is worth noting that the initial yield strength is calculated by using Eq. (5) which is equal to 0.45 times of the maximum compressive strength and the hydrostatic pressure p' for initial yield strength should also be changed based on the second formula in Eq. (5). The modified three strength surfaces of NSC after exposure to 300, 500 and 700 ºC are shown in Figure 2. It is conspicuous that the modified strength surfaces fit better with the triaxial compression test results. Moreover, it shows that the KCC default values underestimate the maximum strength and initial elastic strength as well as residual strength of concrete that has been exposed to high temperature.

Table 3
NSC strength surfaces parameters after modified.

	a_0	a_1	a_2	a_{1f}	a_{2f}	a_{0y}	a_{1y}	a_{2y}
NSC at 25 °C	1.33E+07	0.4463	1.80E-9	0.4417	2.63E-9	1E+07	0.625	5.72E-09
NSC after 300 °C	8.87E+06	0.4463	3.0E-9	0.4417	3.0E-9	6.7E+06	0.625	1.5E-08
NSC after 500 °C	5.03E+06	0.4463	3.1E-9	0.4417	3.3E-9	3.79E+06	0.625	1.0E-08
NSC after 700 °C	8.0E+06	0.4463	4.0E-09	0.4417	4.0E-09	1.0E+06	0.625	9.0E-09

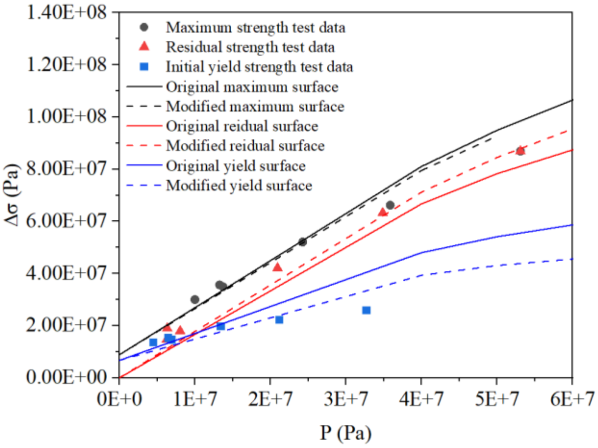

(a) 300 °C

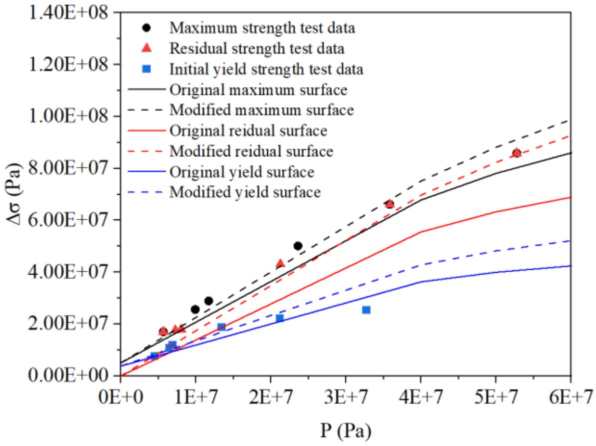

(b) 500 °C

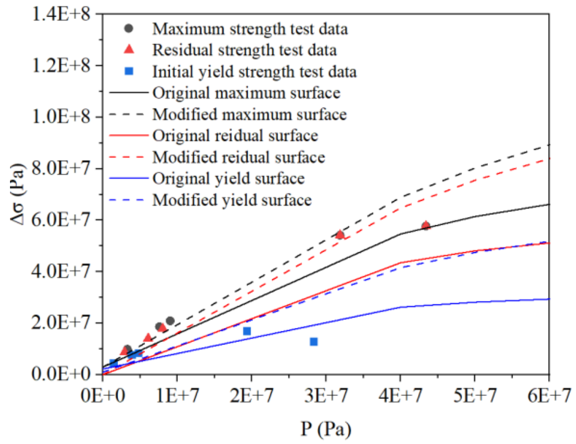

(c) 700 °C

Figure 2. Triaxial compression behaviour of NSC after exposure to various temperatures.

The UHPC triaxial test data at different target temperatures of 200, 400, 600 and 800 °C was adopted in the current study in accordance with the previous study from Xu et al. [49]. Steel slag instead of quartz sand as coarse aggregate was employed in the present mix design to improve fire resistance. At the same time, to enhance the compressive strength, bonding strength, and resistance to abrasion, silica fume was added. The modified a_0, a_2, a_{2f}, a_{0y} and a_{2y} at different target temperatures are listed in table 4. More details in relation to the triaxial compression data and three modified strength surfaces of UHPC after exposure to different temperatures can be found in literature [46].

Table 4

Modified UHPC strength surfaces parameters [46].

	a_0	a_1	a_2	a_{1f}	a_{2f}	a_{0y}	a_{1y}	a_{2y}
UHPC at 20 °C	3.37E+07	0.4463	7.09E-10	0.4417	6.39E-10	2.90E+07	0.625	1.98E-09
UHPC after 200 °C	3.84E+07	0.4463	7.54E-10	0.4417	6.22E-10	3.01E+07	0.625	1.91E-09
UHPC after 400 °C	4.43E+07	0.4463	7.24E-10	0.4417	5.63E-10	3.30E+07	0.625	1.74E-09
UHPC after 600 °C	3.25E+07	0.4463	7.35E-10	0.4417	6.65E-10	2.63E+07	0.625	2.18E-09

UHPC after 800 ℃	1.77E+07	0.4463	1.35E-09	0.4417	1.25E-09	1.47E+07	0.625	3.90E-09

In the KCC model, tensile strength of concrete after exposure to high temperature is another critical parameter to be considered, which can evaluate the residual tensile strength of concrete structures after exposed to high temperature. In terms of NSC, Chang et al. [50] suggested that the relationship between normalized tensile strength $f_{tr}/\ f_t$ and temperature T from 20 ℃ to 800 ℃ is as follows,

$$\frac{f_{tr}}{f_t} = \begin{cases} 1.05 - 0.0025T, & 20\ ℃ < T \leq 100\ ℃ \\ 0.8 & 100\ ℃ < T \leq 200\ ℃ \\ 1.02 - 0.0011T \geq 0 & 200\ ℃ < T \leq 800\ ℃ \end{cases} \tag{11}$$

where f_{tr} is residual tensile strength after high temperature, f_t=3.2 MPa [51], which is tensile strength for NSC at ambient temperature.

However, the reduction in tensile strength regarding UHPC after exposed to elevated temperature is much lower than NSC because the addition of the polypropylene (PP) fibre and steel fibre completely inhibits the spalling of concrete [52]. Li and Liu [53] confirmed that when the hybrid steel and PP fibres were added to UHPC, the tensile strength almost declined linearly with temperature, and the linear equation is given as,

$$\frac{f_{rT}}{f_T} = 1.02 - 0.88\left(\frac{T}{1000}\right) \qquad 20\ ℃ < T < 900\ ℃ \tag{12}$$

where f_{rT} and f_T are residual tensile strength after high temperature and tensile strength at ambient temperature which is equal to 7.7 MPa, respectively.

2.1.2 Relationship between λ and η

To characterise the hardening and softening of strength for NSC in compressive and tensile meridian, a default relationship between the modified effective plastic strain λ and the strength scale factor η is employed [54]. Additionally, a new modified λ-η relationship is created to satisfy the present UHPC. Table 5 presents both the NSC and current UHPC λ-η relationships.

Table 5

NSC and UHPC relationships between λ and η in the KCC model.

NSC λ-η relationship		UHPC λ-η relationship [46]	
λ	η	λ	η
0.0	0.0	0.0	0.0
8E-06	0.85	8E-06	0.85
2.4E-05	0.97	2.4E-05	0.97
4E-05	0.99	4E-05	0.99
5.6E-05	1	5.6E-05	1
7.2E-05	0.99	7.2E-05	0.99
8.8E-05	0.97	8.8E-05	0.97
3.2E-04	0.5	2.5E-04	0.8
5.2E-04	0.1	6.2E-04	0.5
5.7E-04	0.0	1.1E-03	0.3
1.0	0.0	2E-03	0.1
10	0	5E-03	0.0
1E+10	0	1E+10	0.0

2.1.3 Damage accumulation parameters

As mentioned earlier, the modified effective plastic strain λ is to account for damage accumulation under both compression and tension. The formula can be defined as follows,

$$\lambda = \begin{cases} \int_0^{\overline{\varepsilon^p}} \frac{d\overline{\varepsilon^p}}{r_f(1+p/r_f f_t)^{b_1}} & \text{for } p \geq 0 \\ \int_0^{\overline{\varepsilon^p}} \frac{d\overline{\varepsilon^p}}{r_f(1+p/r_f f_t)^{b_2}} & \text{for } p < 0 \end{cases} \tag{13}$$

where r_f is the rate enhancement factor (DIFs), $d\bar{\varepsilon}^p$ is the effective plastic strain increment, b_1 controls the damage and softening behaviour of stress-strain curve in uniaxial compression and b_2 governs the damage and softening behaviour of stress-strain curve in tension.

Wu and Crawford [54] also demonstrated that the data from the uniaxial compression test is fitted to obtain b_1 regularization, while b_2 can be generated by fitting numerical fracture energy which can be obtained from tensile test. In this study, b_1 is equal to 0.25, 1.00, 0.35, 0.65 and 0.70 after exposure to the target temperature of 20, 200, 400, 600 and 800 ºC for the current UHPC, whereas b_1 =1.6 for all temperatures for NSC. b_2 is assumed to be 1.35 for both NSC and UHPC at all temperatures.

There is another damage evolution parameter in the KCC model ω which is an associativity parameter that controls volume expansion in shear dilatancy modelling. The element size and discretization do have an impact on ω selection, albeit the effect is not entirely deterministic. Previous studies have found that the effective value of ω is between 0.50 and 0.90. The recommended value for well-confined and NSC concrete components is 0.80 or 0.90, concrete components with poorly confined and without coarse aggregate is 0.5 or 0.75, whereas high-strength or UHPC concretes with fine aggregate is less than 0.5 [54]. Hence, ω =0.8 for NSC in the following model validation and ω is taken as 0.5 for UHPC.

2.1.4 Strain rate sensitivity

Strain rate can affect the dynamic behaviour of materials. DIF can be determined as the ratio between the dynamic strength and the static strength, which is utilised to describe the strength enhancement of materials under high strain rate. Despite the strain rate sensitivity of concrete decreasing at high temperature, the dynamic compressive strength of concrete increases with strain rate [9].

The dynamic strength behaviour of NSC can be defined by CEB [55], which is given as follows,

$$\frac{f_{c,imp}}{f_{cm}} = \begin{cases} (\dot{\varepsilon}_c/\dot{\varepsilon}_{co})^{1.026\alpha_s}, & 3\times10^{-5} \leq \dot{\varepsilon}_c \leq 30\ s^{-1} \\ \gamma_s(\dot{\varepsilon}_c/\dot{\varepsilon}_{co})^{1/3}, & 30 \leq \dot{\varepsilon}_c \leq 300\ s^{-1} \end{cases} \tag{14}$$

where $f_{C,imp}$ represents the dynamic strength, f_{cm} is static strength, $\dot{\varepsilon}_c$ is strain rate and $\dot{\varepsilon}_{co}$ is quasi-static strain rate, which is equal to $30\times10^{-6}\ s^{-1}$. $\log\gamma_s = 6.156\,\alpha_s - 2$, where $\alpha_s = 1 + (5 + \frac{9f_{cm}}{f_{cmo}})$, $f_{cmo} = 10$ MPa.

After exposure to elevated temperatures and cooling down to ambient temperature, the NSC rate sensitivity is adopted from the compressive strength test data [28], as shown in Table 6.

Table 6

NSC strain rate sensitivity after various temperatures [28].

20 ºC		100 ºC		300 ºC		500 ºC		700 ºC	
Strain rate	DIF	Strain rate	DIF	Strain rate	DIF	Strain rate	DIF	Strain rate	DIF
0	1	0	1	0	1	0	1	0	1
71.4	2.34	58	1.59	67.9	1.76	71.5	1.70	80.3	1.15
78.6	2.42	132.8	2.06	97.5	1.97	78.1	1.75	84.2	1.16
100.1	2.62	-	-	137.8	2.19	128.2	1.81	115.7	1.26

-	-	-	-	148.8	2.24	161.3	2.18	136.1	1.32

For UHPC, Xu et al. [46] obtained the compressive strength DIF values of UHPC after exposure to different target temperatures by curve fitting the experimental data of Liang [30], as shown in Table 7. The data listed below is adopted to predict the impact resistance of UHPC after high temperature in the following simulation.

Table 7
UHPC strain rate sensitivity after various temperatures [30].

20 ºC		200 ºC		400 ºC		600 ºC		800 ºC	
Strain rate	DIF	Strain rate	DIF	Strain rate	DIF	Strain rate	DIF	Strain rate	DIF
0	1	0	1	0	1	0	1	0	1
98.1	1.218	134	1.024	112	1.040	112	1.125	151.7	1.106
147	1.405	246	1.255	164.3	1.102	135.7	1.243	192.7	1.144
206	1.423	362	1.384	203.3	1.116	192.5	1.279	243.3	1.219
258	1.597	-	-	249	1.160	245.5	1.416	292.0	1.316
308.3	1.623	-	-	282.3	1.331	-	-	-	-

2.1.5 Equation of state (EOS)

Equation of state (EOS) TABULATED_COMPACTION is used to explain the relationship between pressure and volumetric strain in the KCC model. The pressure is defined as Eq. (15) following below. Normally, the uniaxial compressive strength can be utilised to automatically generate the EOS of NSC, which is listed in Table 8.

$$p = C(\mu) + \gamma_0 \theta(\mu) E_0 \tag{15}$$

where γ_0 is the ratio of specific heat, and E_0 is presented as the internal energy per initial volume. $C(\mu)$ is the input pressure from EOS assessed along a 0 K isotherm and $\theta(\mu)$ is thermal coefficient with respect to volumetric strain function, respectively.

In the present model for UHPC, a piecewise EOS is described as follows,

$$\begin{cases} p = K\mu & p < p_{crush} \\ p = p_{crush} + K_{lock}(\mu - \mu_{crush}) & p_{crush} < p < p_{lock} \\ p = K_1\overline{\mu} + K_2\overline{\mu}^2 + K_3\overline{\mu}^3 & p > p_{lock} \end{cases} \tag{16}$$

where p_{crush} is the pressure at the first EOS slope change point, whereas p_{lock} is the second slope change point. The elastic bulk modulus $K = p_{crush}/\mu_{crush} = \frac{E}{3(1-2v)}$, where v is presented as the Poisson's ratio and E is the modulus of elasticity. $K_{lock} = (p_{lock} - p_{crush})/(\mu_{plock} - \mu_{crush})$ where μ_{plock} is the volumetric strain for p_{lock} and $\overline{\mu} = (\mu - \mu_{lock})/(1 + \mu_{lock})$, where $\mu_{lock} = \frac{\rho_{grain}}{\rho_o} - 1$ (ρ_{grain} is the density after compaction and ρ_o is the original density).

Concrete density ρ is influenced by water loss at various temperatures. ρ=2400 kg/m^3 at ambient temperature is used in the present study. Eurocode 2 [56] suggests that the concrete density at different temperatures can be determined as follows,

$$\rho(\theta) = \begin{cases} \rho(20\ ℃) & for\ 20\ ℃ \le \theta \le 115\ ℃ \\ \rho(20\ ℃) \cdot \left(1 - \frac{0.02(\theta - 115)}{85}\right) & for 115\ ℃ < \theta \le 200\ ℃ \\ \rho(20\ ℃) \cdot \left(0.98 - \frac{0.03(\theta - 200)}{200}\right) & for 200\ ℃ < \theta \le 400\ ℃ \\ \rho(20\ ℃) \cdot \left(0.95 - \frac{0.07(\theta - 400)}{800}\right) & for 400\ ℃ < \theta \le 1200\ ℃ \end{cases} \quad (17)$$

In the current study, v is taken as 0.15 and 0.18 for NSC and UHPC at room temperature, respectively. In addition, modulus of elasticity is relative to uniaxial compressive strength (f_c). According to the ACI building code [57], the elastic modulus of NSC can be presented as $E = 4730\sqrt{f_c}$ in MPa, whereas the elastic modulus of UHPC can be defined as $E = 3840\sqrt{f_c}$ in MPa [58]. The guideline for the modulus of elasticity with respect to NSC and UHPC in various temperatures recommended by [59-61] is shown in Figure 3.

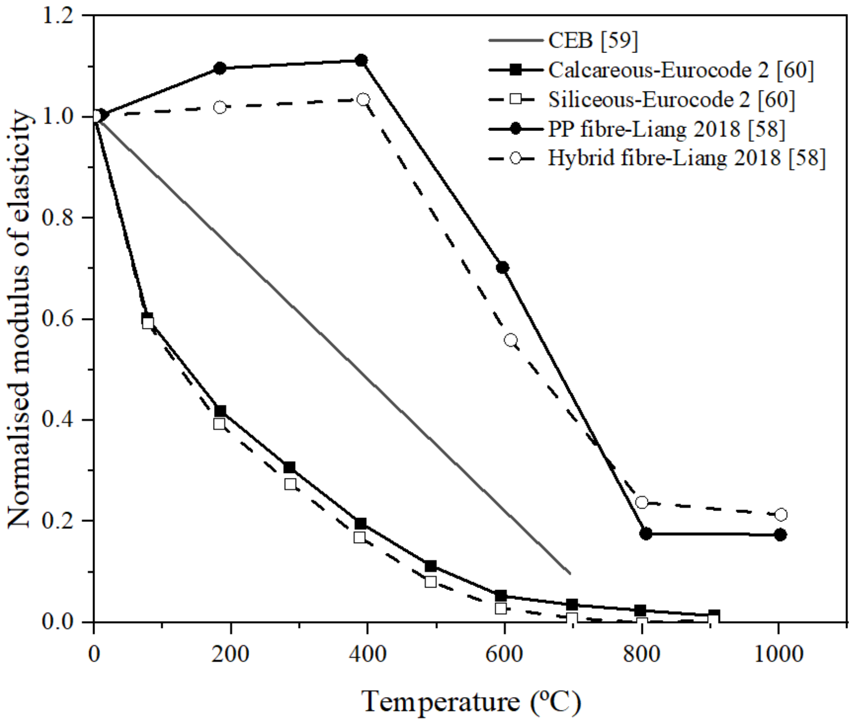

Figure 3. Degradation of elastic modulus in high temperatures [46].

It is obvious that there is a big deviation between the KCC default EOS and experimental test data for UHPC (which uniaxial compressive strength was 94.64 MPa) from Figure 4 (a). Therefore, the EOS of UHPC is modified in the present study. The linear elastic stage, transition stage, and compact stage are the three stages that characterise the EOS of concrete. At the first stage (when $p < p_{crush}$), EOS is followed by Eq.(16) and the elastic limit pressure p_{crush}=0.25 GPa is adopted based on the study by Neel [62]. In the second stage, the pressure of the second slope change point p_{lock}=1.5 GPa is adopted from Erzar et al. [63]. At compact stage (when $p > p_{lock}$), by fitting the experimental data [62, 64] followed by Eq.(18), K_1=184599, K_2=-1660709 and K_3=7177252 are adopted. In terms of the unloading bulk modulus (K), it can be automatically generated in the KCC model in the first stage of EOS. After the elastic limit, K can be obtained by using volumetric scaling method [38] which means employing the proportion between the automatically generated and adjusted elastic bulk modulus for both NSC and UHPC. Tables 8 and 9 illustrate the full definitions of the updated EOSs for various temperatures in relation to NSC and UHPC, respectively.

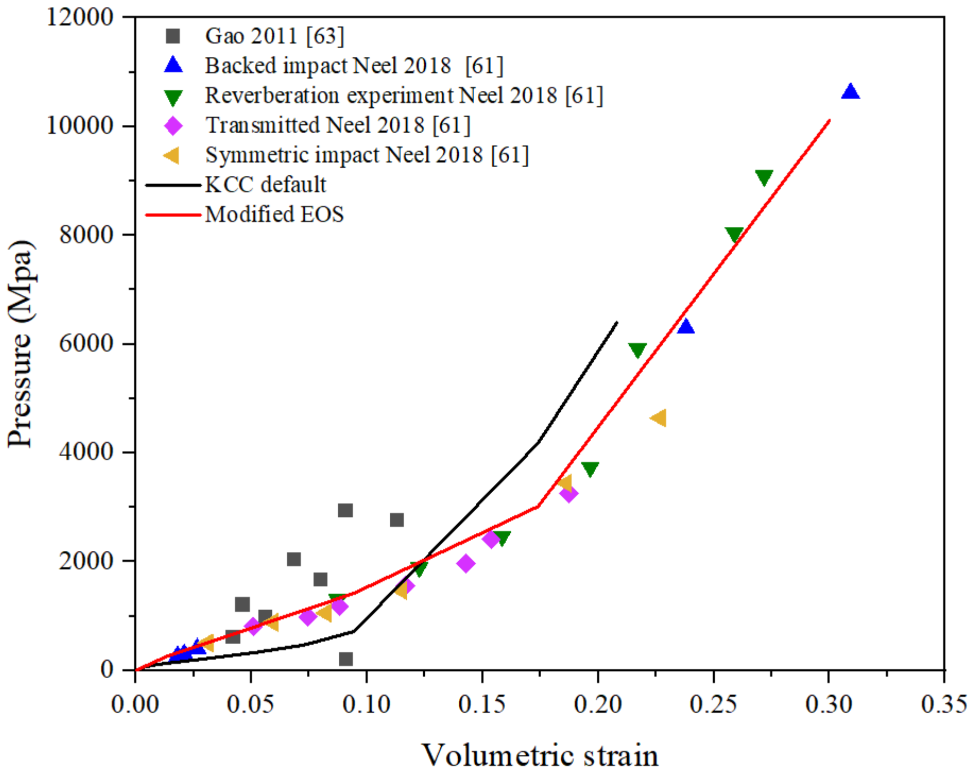

(a)

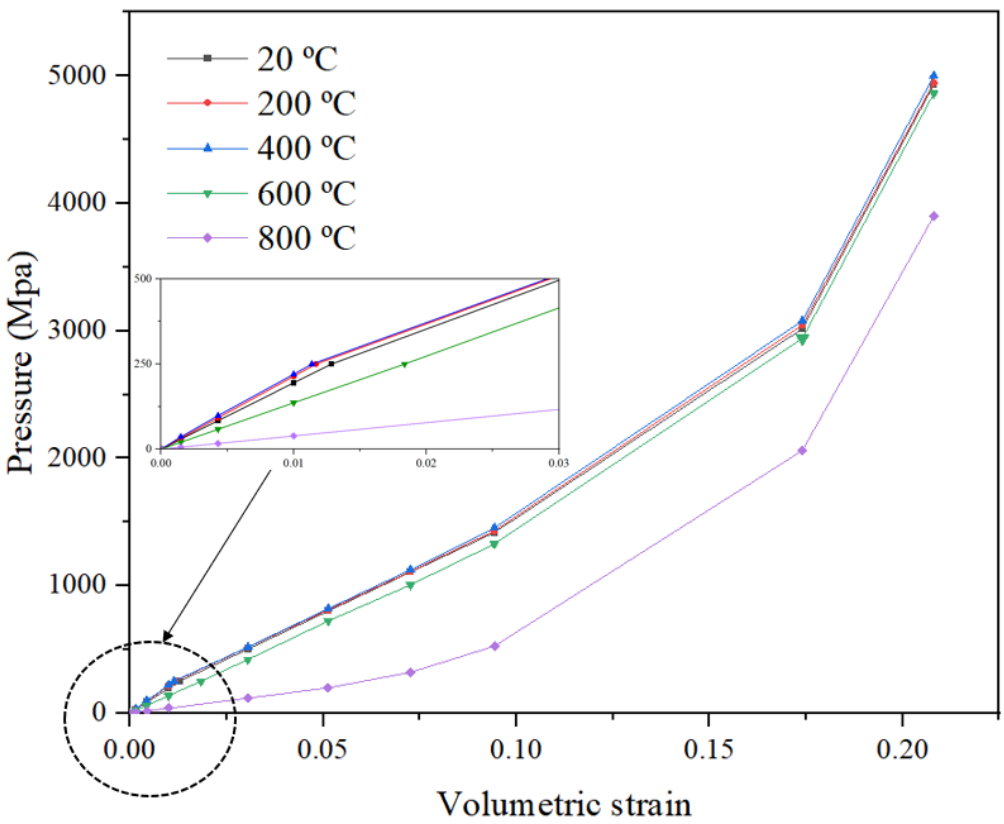

(b)

Figure 4. Pressure-volumetric strain curve for UHPC. (a) Experimental data and KCC default EOS (b) EOS prediction in various temperature

Table 8

EOS for NSC after exposure to various temperatures.

20 ºC (Default)	μ	0	-0.0015	-0.0043	-0.01	-0.0305	-0.0513	-0.0726	-0.0943	-0.174	-0.208
	C (MPa)	0	22.68	49.445	79.38	150.83	227.49	322.76	493.77	2883	4409
	K (GPa)	15.12	15.12	15.33	16.10	19.16	22.23	25.28	27.60	62.09	75.60
300 ºC	μ	0	-0.0015	-0.0043	-0.01	-0.0305	-0.0513	-0.0726	-0.0943	-0.174	-0.208
	C (MPa)	0	18.52	40.37	64.82	123.15	185.75	263.53	403.16	2354	3600
	K (GPa)	12.35	12.35	12.52	13.15	15.64	18.15	20.45	22.54	50.72	61.75
500 ºC	μ	0	-0.0015	-0.0043	-0.01	-0.0305	-0.0513	-0.0726	-0.0943	-0.174	-0.208
	C (MPa)	0	13.94	30.39	48.79	92.71	139.8	198.4	303.5	1772	2710
	K (GPa)	9.29	9.29	9.42	9.90	11.78	13.66	15.54	16.96	38.15	46.45
700 ºC	μ	0	-0.0015	-0.0043	-0.01	-0.0305	-0.0513	-0.0726	-0.0943	-0.174	-0.208
	C (MPa)	0	10.64	23.19	37.23	70.75	106.7	151.39	231.6	1352	2068
	K (GPa)	7.09	7.09	7.19	7.55	8.99	10.43	11.86	12.94	29.12	35.45

Table 9

EOS for UHPC after exposure to various temperatures.

20 ºC	μ	0	-0.0016	-0.0043	-0.01	-0.0305	-0.0513	-0.0726	-0.0943	-0.174	-0.2
	C (MPa)	0	29.18	83.66	194.6	503.2	801.5	1107	1418.2	3016.4	4930
	K (GPa)	20.8	20.8	21.09	22.15	28.07	30.57	34.78	37.96	85.42	104
200 ºC	μ	0	-0.0016	-0.0043	-0.01	-0.0305	-0.0513	-0.0726	-0.0943	-0.174	-0.2
	C (MPa)	0	32.10	92.03	214.0	516.4	810.7	1112.2	1430.4	3046.5	4946
	K (GPa)	23.64	23.64	23.97	25.18	31.90	34.75	39.52	43.14	97.08	118.2
400 ºC	μ	0	-0.0016	-0.0043	-0.01	-0.0305	-0.0513	-0.0726	-0.0943	-0.174	-0.2
	C (MPa)	0	32.98	94.54	219.9	519.8	820.2	1125.6	1453.3	3078.5	4999
	K (GPa)	26	26	26.36	27.69	35.08	38.22	43.47	47.45	106.8	130
600 ºC	μ	0	-0.0016	-0.0043	-0.01	-0.0305	-0.0513	-0.0726	-0.0943	-0.174	-0.2
	C (MPa)	0	20.43	58.56	136.2	421.9	724.4	1006.5	1326.8	2941.2	4862
	K (GPa)	12.64	12.64	12.81	13.46	17.05	18.58	21.13	23.07	51.91	63.18
800 ºC	μ	0	-0.0016	-0.0043	-0.01	-0.0305	-0.0513	-0.0726	-0.0943	-0.174	-0.2
	C (MPa)	0	5.84	16.73	38.91	118.7	199.6	320.9	526.7	2060.6	3898
	K (GPa)	6.54	6.54	6.63	6.97	8.82	9.61	10.93	11.94	25.86	32.69

2.2 Thermal conductivity of concrete

Heat transfer analysis can be adopted to estimate the transient temperature distribution of concrete structural elements exposed to fire. The time-dependent temperature at exposed surface in heat transfer can be determined by the ISO-834 fire curve [65],

$$T_{ISO} = 20 + 345 \log_{10}(8t + 1)$$

where T_{ISO} is the temperature in degree Celsius (ºC), t is time in minute.

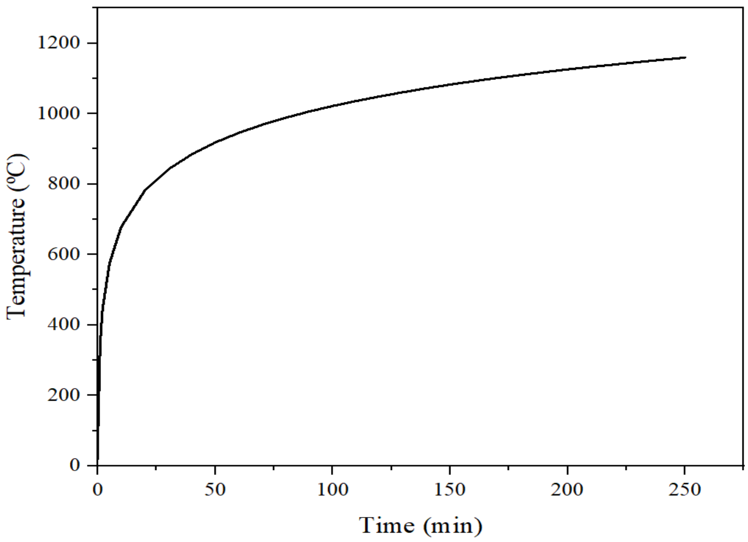

Figure 5. Standard ISO-834 fire curve.

When a real fire occurs, the concrete wall/slab is exposed from one side, resulting in thermal gradient within the concrete structure. To determine the internal temperature, ASTM E119 develops curves describing the temperature at different depths over time [66], as shown in Figure 6.

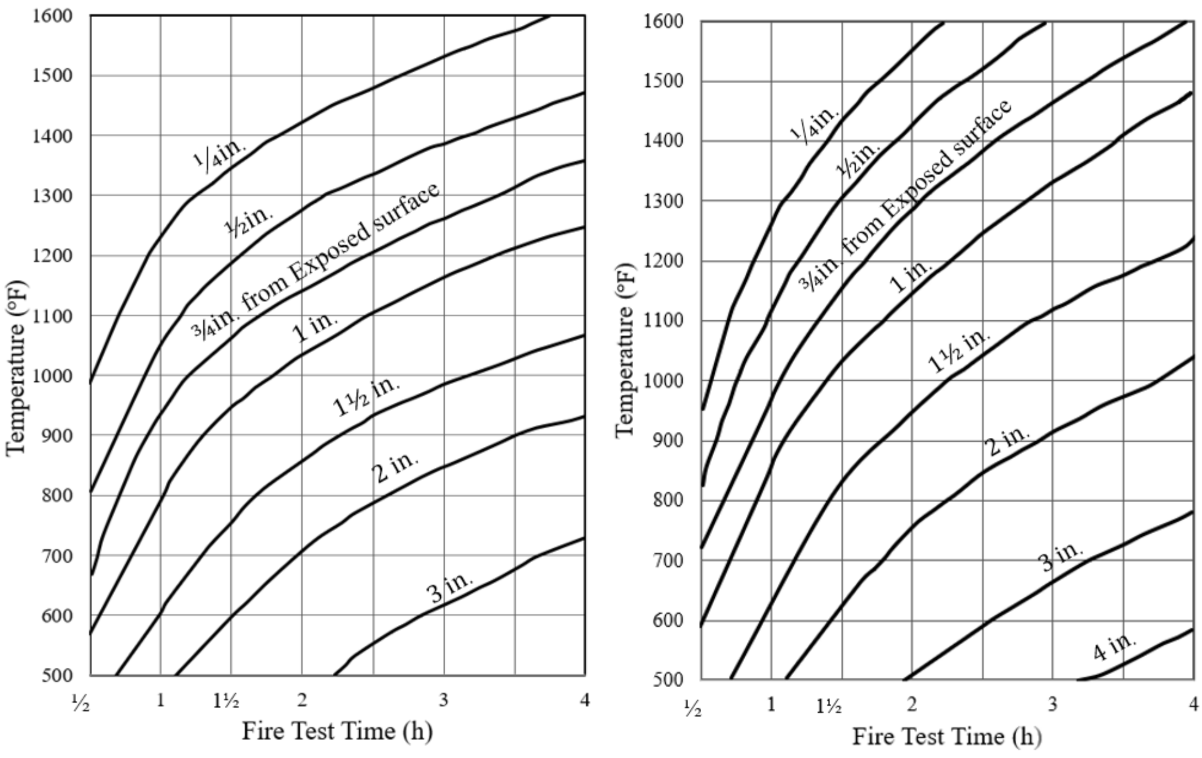

(a) Carbonate aggregate concrete (b) Siliceous aggregate concrete

Figure 6. Temperatures of concrete slab/panel during the fire exposed in different aggregate (ASTM E119 reported by Banerjee [67]).

2.3 Steel reinforcements model

2.3.1 Temperature degradation effect

The characteristics of reinforcement such as yield strength and tensile strength are dramatically impacted by high temperatures. According to the statistical analysis conducted by Tao et al. [68], the yield strength is not affected by heating when the temperature is lower than 500 °C, while the average yield strength loss of reinforcement is approximately 19.4% at 800 °C. The following formula predicts the loss of yield strength with respect to reinforcing steel at different temperatures,

$$f_{yT}=\begin{cases} f_y & T\leq 500\ ℃ \\ [1-5.82\times10^{-4}(T-500)]f_y & T>500\ ℃ \end{cases} \tag{18}$$

where f_{yT} represents residual yield strength after fire, while f_y = 480 MPa is yield strength of reinforcing steel at room temperature.

When the temperature exceeds 500 °C, the elastic modulus of reinforcement tends to decrease slightly. After reaching to 1000 °C, the modulus of elasticity is expected to decrease by 6.5%. In the present study, a model that predicts the modulus of elasticity with the increasing temperature adopted from [68] is suggested as,

$$E_{sT}=\begin{cases} E_s & T\leq 500\ ℃ \\ [1-1.30\times10^{-4}(T-500)]E_s & T>500\ ℃ \end{cases} \tag{19}$$

where E_{sT} represents modulus of elasticity after fire, while E_s =200 GPa is modulus of elasticity with regard to reinforcing steel at ambient temperature.

2.3.2 Strain rate effect

The yield and ultimate tensile DIFs that suggested by CEB [69] are provided as follows,

$$\mathrm{YDIF}=\frac{f_y}{f_{y0}}=1.0+\left(\frac{6.0}{f_{y0}}\right)\ln\left(\frac{\dot{\varepsilon_s}}{\dot{\varepsilon_{s0}}}\right) \tag{20}$$

$$\mathrm{UDIF}=\frac{f_u}{f_{u0}}=1.0+\left(\frac{7.0}{f_{u0}}\right)\ln\left(\frac{\dot{\varepsilon_s}}{\dot{\varepsilon_{s0}}}\right) \tag{21}$$

where f_y is the dynamic yield strength and f_u is presented as ultimate tensile strength, f_{y0} and f_{u0} are static yield strength and ultimate tensile strength in MPa, $\dot{\varepsilon_s}$ is strain rate and $\dot{\varepsilon_{s0}}$ is strain rate at quasi-static state, which is equal to $50\times10^{-5}\ s^{-1}$.

3 Model validation of a post-fire RC slab to impact loading

To assess the accuracy of numerical model in relation to impact behaviour of the post-fire RC slab, the experiment at BARC (Mumbai, India) [35] is adopted. The RC slab has dimension of 1700 mm × 2000 mm with a thickness of 200 mm, and the reinforcement is ϕ10@200 mm (see Figure 7). The RC slab was exposed to the standard fire ISO-834 for about 1 hr from the bottom side and naturally cooled down before impact test. Thermocouples were installed at five different locations along slab thickness to gauge the internal temperature distribution of the slab. The RC slab was then divided into five different layers in various temperatures based on the thermocouples results (see Figure 8). Each layer possessed its own material properties for NSC that discussed in the previous section such as the strength surfaces, λ-η relationships, damage accumulation parameters, DIFs and EOS. A 588 kg punch was dropped from the height of 5 m. The impact velocity can be calculated by $v=\sqrt{2gh}$, which is equal to 9.9 m/s. The punch consisted of three parts, including circular plates from head, cylindrical body with a 170 mm diameter and a smooth spherical head on the impact side with a 191 mm radius. Three groups of mesh size sensitivity tests have been done, including the first group with 8 mm concrete, 2.5 mm reinforcement and 8 mm punch; the second group with 10 mm concrete and 5 mm reinforcement, 10 mm punch; the third group with 20 mm concrete, 10 mm reinforcement and 20 mm punch. To balance the accuracy and computational cost, the element mesh size with the second group was chosen (see Figure 9). The details for all materials are summarised in Table 10.

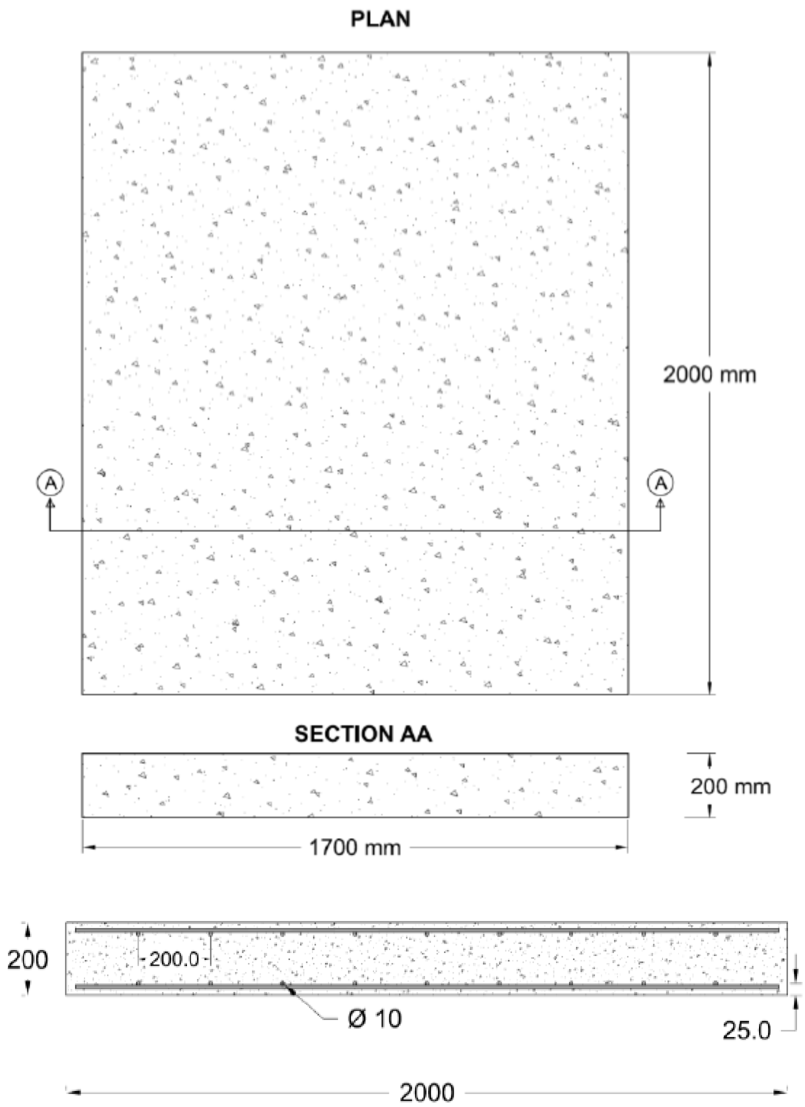

Figure 7. Dimensions of reinforced concrete slab (in mm)[35].

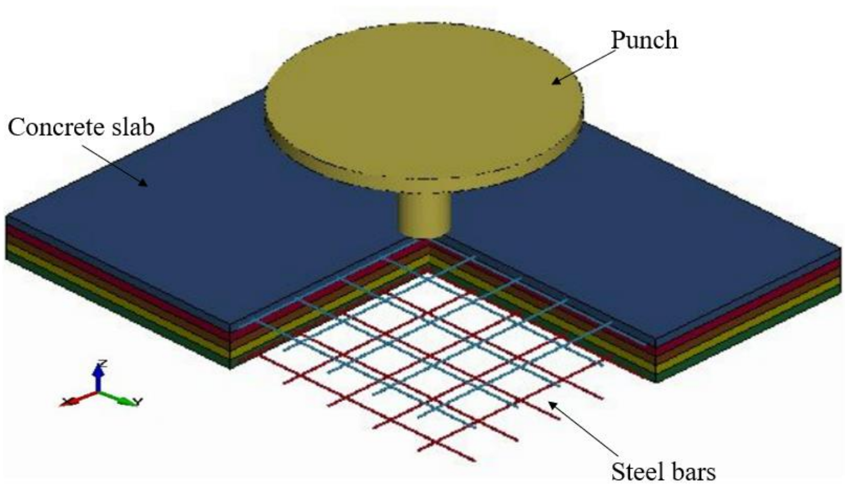

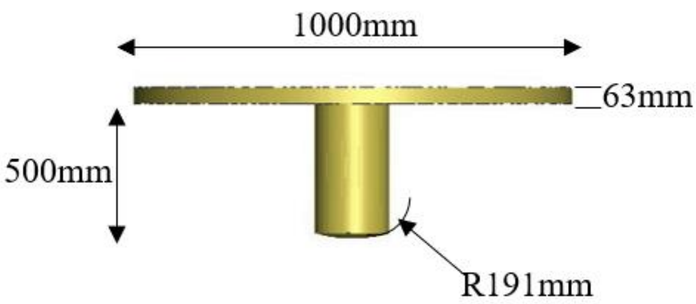

Figure 8. Schematic view of punch-slab system and punch details.

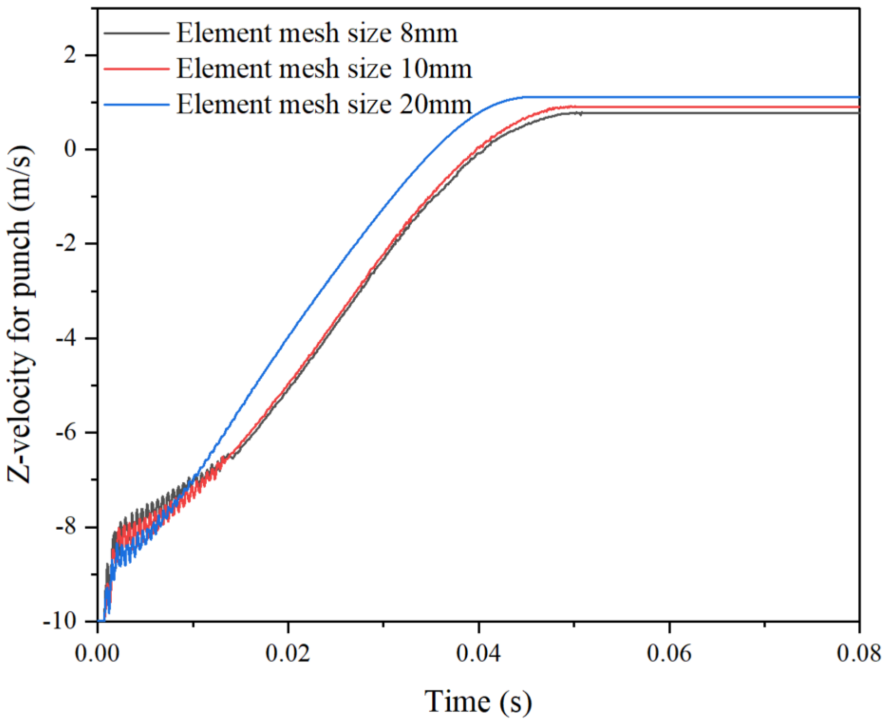

Figure 9. Mesh convergence results of impact loading.

Table 10
Material numerical model and parameters.

Material	LS-DYNA Model	Input Parameters	Magnitude for NSC	Magnitude for UHPC
Concrete	MAT_CONCRETE_ DAMAGE_REL3	Mass Density	2400 kg/m^3	2400 kg/m^3
		Strength parameters	Follow Table 3	Follow Table 4
		λ-η relationship	Follow Table 5	Follow Table 5
		DIF	Follow Table 6	Follow Table 7
		EOS	Follow Table 8	Follow Table 9
	MAT_ADD_EROSION	Maximum principal strain	0.9	0.9
Steel rebar	MAT_PIECEWISE_ LINEAR_PLASTICITY	Mass density	7800 kg/m^3	7800 kg/m^3
		Yield strength	Follow Eq. (18)	Follow Eq. (18)
		Poisson's ratio	0.3	0.3
		Young's modulus	Follow Eq. (19)	Follow Eq. (19)
		Strain rate	Follow Eq. (20) & (21)	Follow Eq. (20) & (21)

Punch	MAT_RIGID	Mass density Young's modulus Poisson's ratio	7800 kg/m^3 200 GPa 0.3	7800 kg/m^3 200 GPa 0.3

The failure patterns from both the top and bottom surfaces are in good accordance with the experimental findings, as can be observed from Figure 10. The RC slab exhibited larger damage area on the bottom surface where radial cracks and extensive fragmentation occurred.

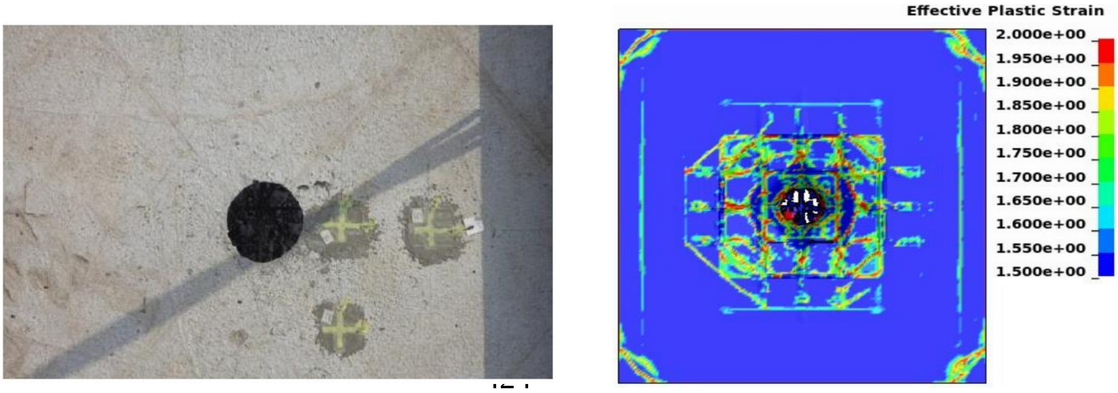

(a) Top surface

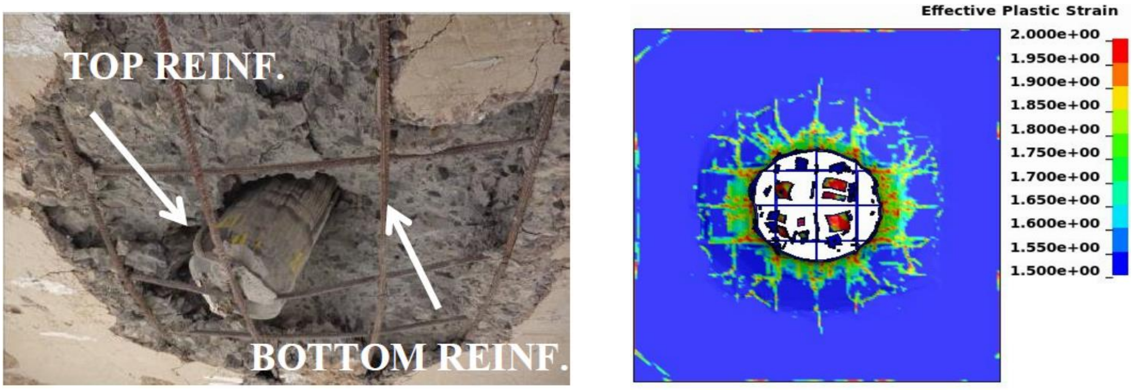

(b) Bottom surface

Figure 10. Failure patterns of RC slab on top and bottom surface.

Furthermore, the strain-time history at strain gauge SG1 was also compared with the experimental results. Two directions of the strain data have been recorded during the experiment, including vertical direction (the strain gauge parallel to the longer RC slab side) and horizontal direction (the strain gauge perpendicular to the longer RC slab side). The data has been recorded since the punch contacted the concrete slab. As can be seen from Figure 11, both vertical and horizontal directions were consistent with the experimental measurements. Therefore, the impact behaviour of the post-fire RC slab can be simulated by using this numerical model.

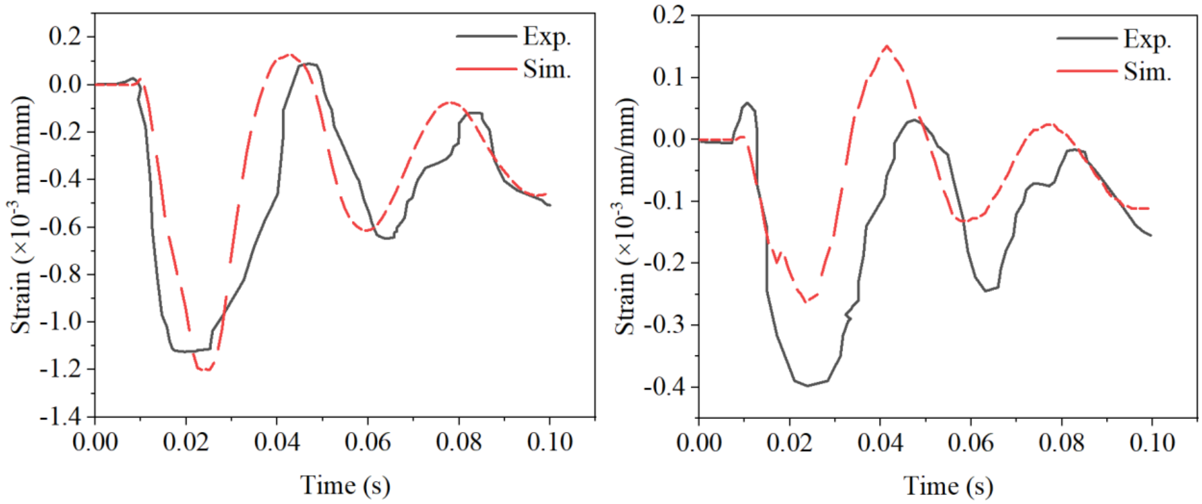

(a) Horizontal direction (b) Vertical direction

Figure 11. Strain- time history of experiment and simulation results with respect to horizontal and vertical direction.

4 Post-fire impact resistance of a reinforced UHPC slab

A reinforced UHPC slab was exposed to fire about 2 hrs in this section. The reinforced UHPC slab was divided into five layers because of the uneven distribution of temperature within the slab. The temperature of the concrete member in different thickness was based on ASTM E119 [66] (see Figure 6). Siliceous aggregate type (refer to Figure 6(b)) was utilized for thermal distribution of UHPC, while the thermal distribution of NSC for each layer was obtained from Figure 6(a) carbonate aggregate concrete. The temperature within each layer chose the nearest value from experimental data [37, 44] due to the limited triaxial concrete test after exposure to different elevated temperatures. In addition to this, the maximum distance from exposed surface to unexposed surfaces of the concrete slab was 4 inches (101.6 mm) in ASTM E119, which was less than thickness in the present study, therefore, room temperature was then used for the first and second top layers. Each layer had a thickness of 40 mm, therefore, the temperature of the first, second and third last layer would choose ¾ inches (19.05 mm), 3 inches (76.2 mm) as well as 4 inches (101.6 mm) (refer to Figure 6). The temperature for each layer is presented in Figure 12.

(a)

(b)

Figure 12. Temperature distribution for RC slab with 2 hrs fire-exposed time. (a) NSC (b) UHPC

MAT_CONCRETE_DAMAGE_REL3 (KCC model) was adopted to describe different properties of UHPC for each layer. MAT_PIECEWISE_LINEAR_PLASTICITY was utilised for steel rebars in the model, which allowed user-defined arbitrary plastic stress-strain curve with strain rate dependence. This model was widely used when steel bars were affected by impact loadings or high temperature [46, 70, 71]. The properties allow of steel rebars were also changed owing to the effect of high temperature (see Section 2.3). In addition, a 500 kg punch was modelled by MAT_RIGID, which was falling down in 5 m high at 9.9 m/s impact velocity. The material properties employed in this numerical simulation were summarised in Table 10. Through numerical modelling in LS-DYNA, the damage to the post-fire UHPC slab under impact load would be compared with NSC in the current work.

The failure patterns for both the concrete slabs are presented in Figure 13. Overall, the damage area on the rear side was larger than the top side. It was evident that the UHPC slab was more resistant to local damage than the NSC slab. There was a circular hole on the top side of the NSC slab and the punch penetrated the whole slab, resulting in a large spalling area on the back surface. The punching shear failure area was approximately 0.608 m^2 which was nearly 3.38 times more than UHPC. The top side of UHPC had observable indentation causing by the high velocity punch and there was no spalling on the rear side. Circumferential and radial cracks were developed on the rear side for both the slabs.

Time histories of impact force and the top steel bars mid-point displacement for both the NSC and UHPC slabs are plotted in Figure 14. The peak value was dramatically lower for NCS than that for UHPC, which was 1280 kN and 2000 kN, respectively from Figure 14 (a). It was noted that the impact forces reached peak value very quickly and dropped down sharply. It was important to note that the impact force fluctuated around a certain value during the decrease in impact force, which was also called plateau value. The plateau impact force was significantly larger in UHPC than NSC. Moreover, the impact duration of NSC was shorter than UHPC as the punch penetrated the whole NSC slab quickly. The impact force after 2.2 ms in NSC shown in Figure 14 (a) was probably owing to the contact between indenter and reinforcement. The impulse experienced by UHPC was approximately 5.12 kN·s, while NSC was about 1.75 kN·s. The maximum steel bars mid-point displacement for NSC was nearly 160 mm, which was 2.7 times more than that for UHPC. In addition, the residual deflection for NSC was 58 mm and approximately 150 mm for UHPC (see Figure 14 (b)). These once more demonstrated that UHPC had substantially higher local impact resistance than NSC.

In general, it is evident that the UHPC slab demonstrated greater impact resistance in comparison to the NSC slab after exposure to fire for two hrs with respect to failure patterns, higher peak impact force and plateau value, less impact duration as well as lower mid-point deflection.

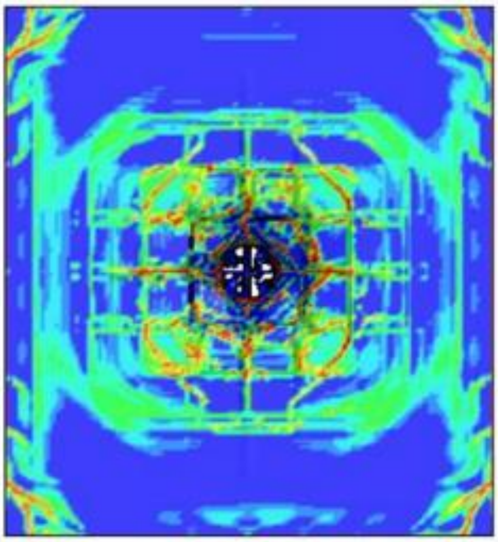

(a) Top surface for NSC

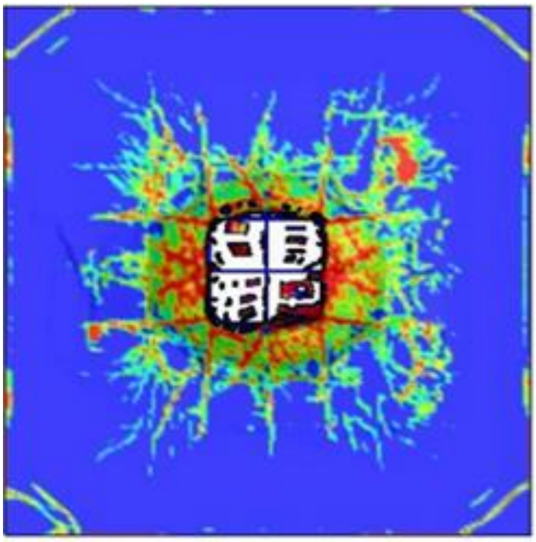

(b) Bottom surface for NSC

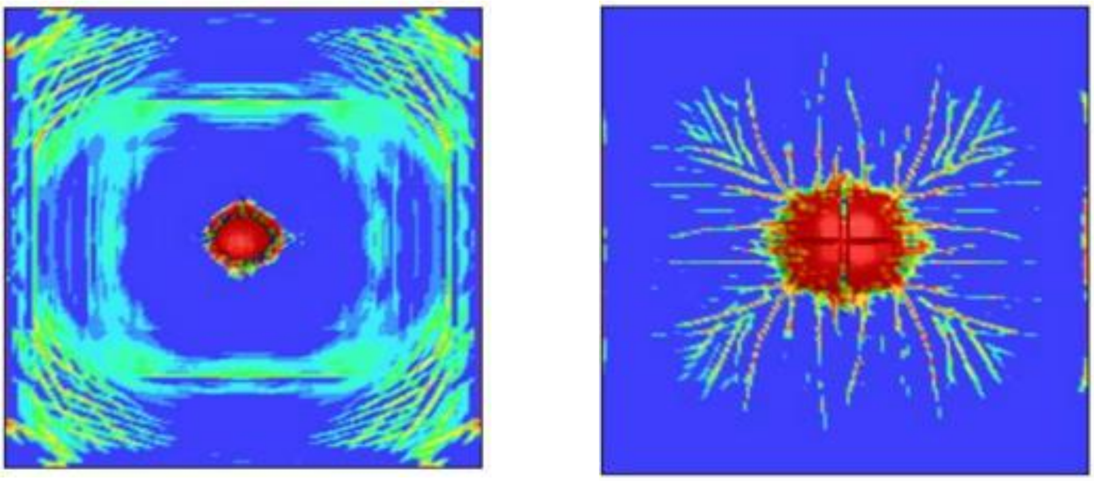

(c) Top surface for UHPC (d) Bottom surface for UHPC

Effective Plastic Strain 1.5 **2.0**

Figure 13. Failure patterns of NSC and UHPC on the top and bottom surface.

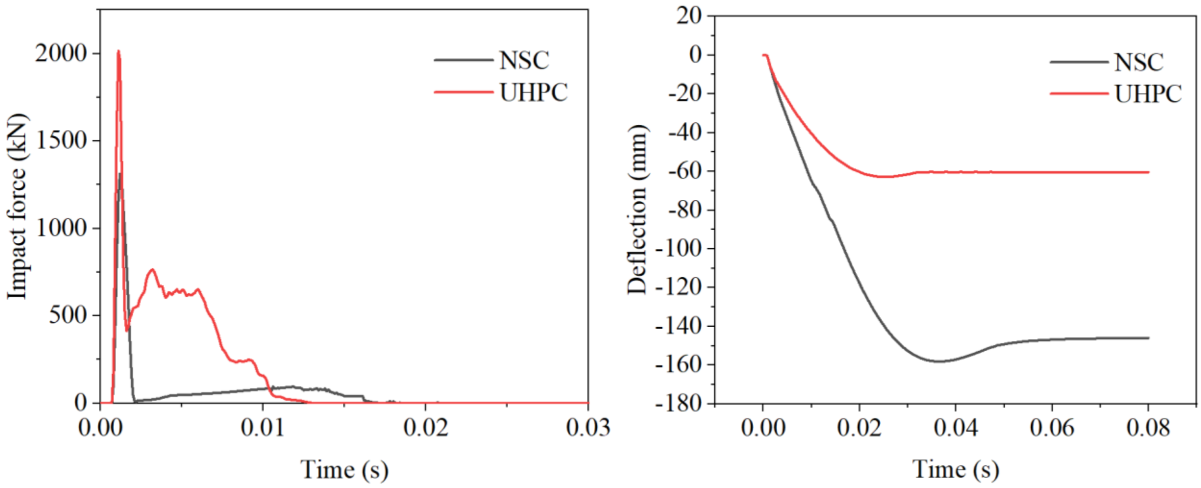

(a) Impact (b) Deflection

Figure 14. Time history of impact force and deflection for NSC and UHPC.

5 Parametric Study

Based on the model comparison above, the parametric analysis was developed herein to carry out the influence of different parameters on impact behaviour of both the reinforced NSC and UHPC slabs after exposure to elevated temperatures. The material models and the size of tested specimens were the same as those in Sections 3 and 4. In this section, the investigated parameters included fire-exposed time, impact velocity and impact mass.

5.1 Fire-exposed time

Both the NSC and UHPC slabs were exposed to fire for 1, 2, 3 and 4 hrs to explore the impact behaviour via numerical simulation. Impact mass for all the tested groups was 500 kg and the punch dropped in 5 m height, i.e. impact velocity of 9.9 m/s. The temperature distribution of concrete member in different thickness was based on ASTM E119 [66] (see Figure 6), and Figure 15 displays the temperature distribution for both NSC and UHPC with different fire-exposure time .

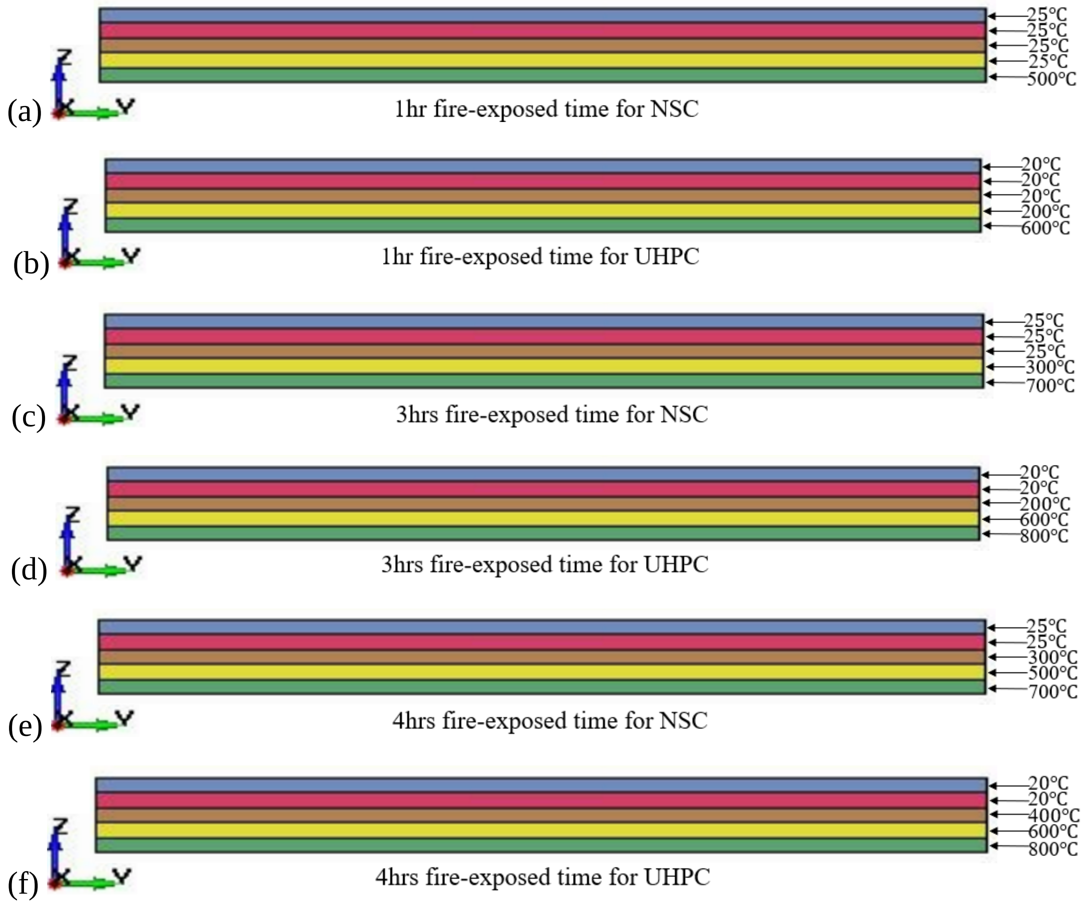

Figure 15. Temperature distribution of NSC and UHPC after different fire-exposed time.

The failure patterns of the RC slabs are illustrated in Figure 16. It demonstrated that the damage area was increasing with the fire-exposed time. In addition, the spalling area for NSC was becoming increasingly larger with longer exposure time to fire. The circumferential cracks for the UHPC slabs were much longer and wider. It was obvious that the localized damage was highly dependent on the fire-exposed time. The punching shear failure areas in NSC were 2.5 times, 3.0 times and 1.2 times larger than UHPC after exposure to fire at 1 hr, 3 hrs and 4 hrs, respectively (see Figures 16 &18). Impact force for NSC and UHPC at different fire-exposed time is presented in Figure 17. It indicated that the impact force decreased with the increase in fire-exposed time. In general, the peak impact force for UHPC is visibly higher than NSC. In addition to this, the impulse for UHPC was signally larger than NSC. The impulse experienced by NSC at 1 hr, 3 hrs and 4 hrs were 1.72 kN·s, 1.78 kN·s (increased 3.4%) and 2.4 kN·s (increased 39.0%), respectively. The impulse experienced by UHPC at 1 hr, 3 hrs and 4 hrs were 3.3 kN·s, 5.1 kN·s (increased 54.2%) and 5.2 kN·s (increased 56.5%), respectively (see Figure 18).

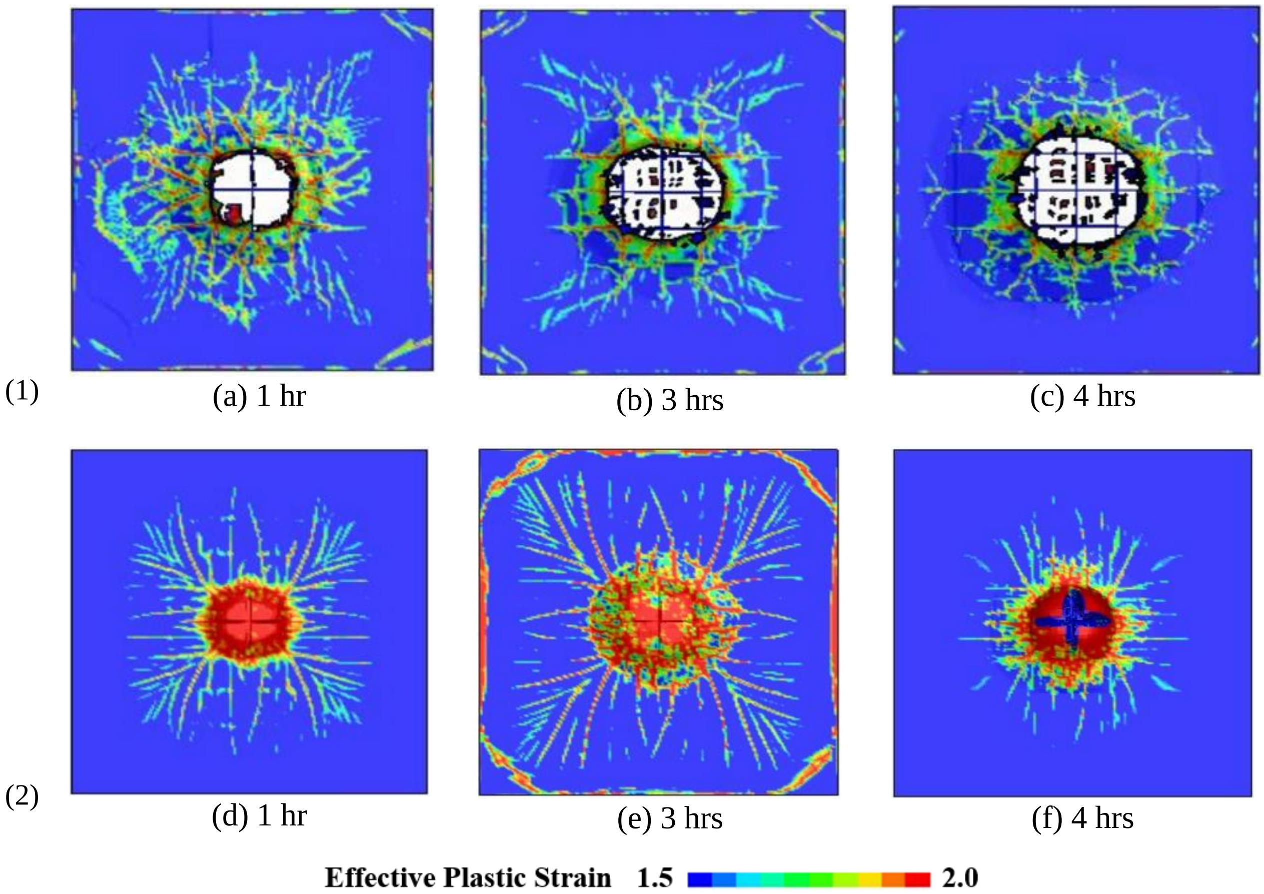

Figure 16. Final failure patterns of slabs on bottom side subjected to impact force in different fire-exposed time. (1) NSC (2) UHPC

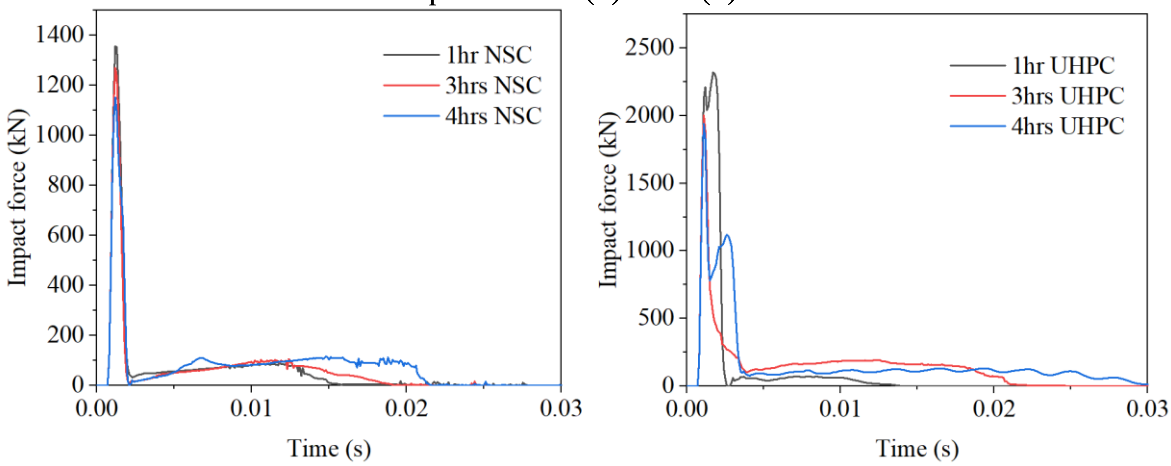

(a) NSC (b) UHPC

Figure 17. Impact force for NSC and UHPC at different fire-exposed time.

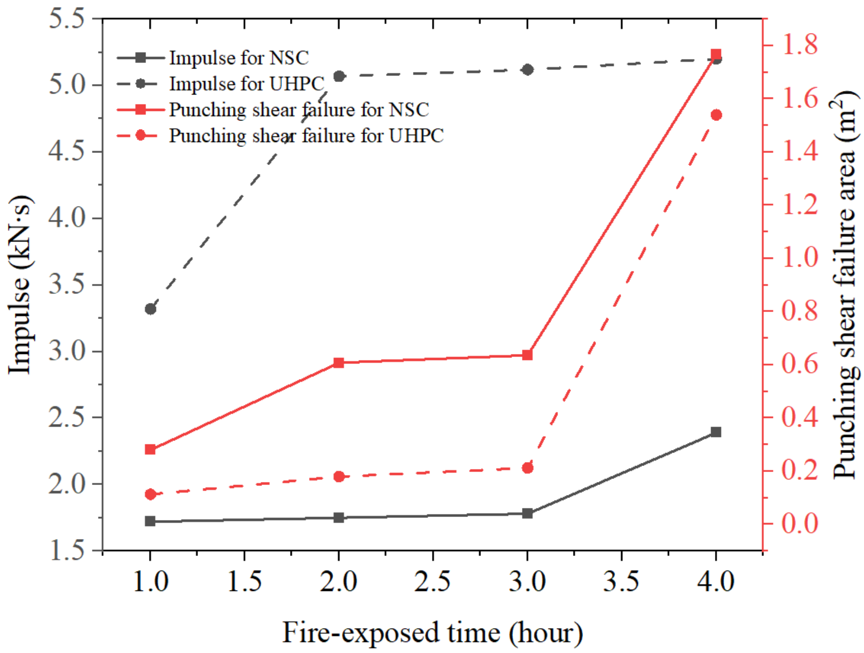

Figure 18. Impulse and punching shear failure area for both NSC and UHPC after exposure to elevated temperature.

5.2 Impact velocity

To evaluate the influence of impact velocity with respect to the post-fire slabs, four different impact velocity groups were tested, including 4.4 m/s (falling height 1 m), 7.7 m/s (falling height 3 m), and 9.9 m/s (falling height 5 m) as well as 11.7 m/s (falling height 7 m). All of the tested specimens were conducted to the standard fire exposure of 2 hrs and the impact mass was 500 kg in the test. The final failure patterns of NSC on the bottom side in different impact velocities are presented in Figure 19. It demonstrated that the damage area of the NSC slab increased with the higher impact velocity. No concrete scabbing and radical crack were observed when the impact velocity was equal to 4.4 m/s. After increasing to 11.7 m/s, the concrete spalled on the bottom side. In terms of the UHPC slab, limited mass penetration was observed on the top surface (see Figure 20). Moreover, it was noted that the impact area increased after increasing the impact velocity. Higher impact velocity would lead to more localised damage. The punching shear failures on the bottom side of NSC were 1.3 times, 4.1 times and 4.7 times more than UHPC at 4.4 m/s, 7.7 m/s and 11.7 m/s (see Figure 22). Impact forces for NSC and UHPC in different impact velocities are shown in Figure 21. The impact force for UHPC is dramatically higher than NSC. The peak impact forces for NSC at 4.4 m/s, 7.7 m/s and 11.7 m/s were 772 kN, 1118 kN and 1585 kN, respectively. The peak impact forces for UHPC for 4.4 m/s, 7.7 m/s and 11.7m/s were 1160 kN, 1680 kN and 2330 kN, respectively. The peak impact force also increases with the impact velocity. Furthermore, the impulse for NSC at 4.4 m/s, 7.7 m/s and 11.7 m/s were 1.5 kN·s, 1.7 kN·s (increase 13.3%) and 3.7 kN·s (increase 146.7%), respectively. The impulse for UHPC at 4.4 m/s, 7.7 m/s and 11.7 m/s were 3.3 kN·s, 4.5 kN·s (increase 74.3%) and 6.0 kN·s (increase 166%), respectively (see Figure 22).

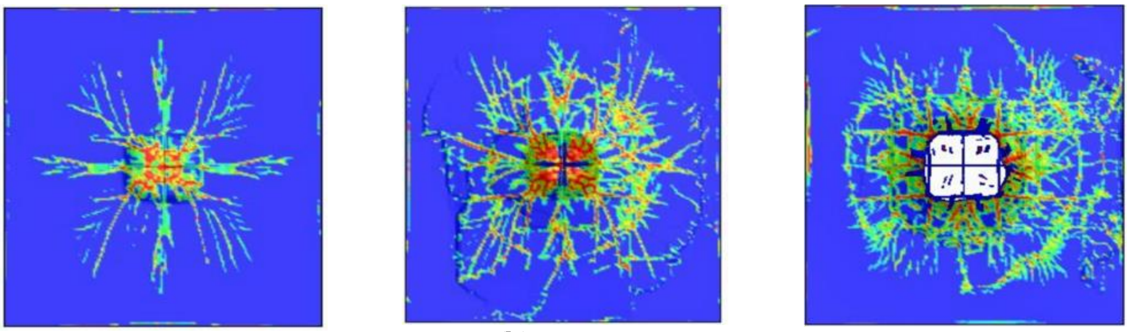

(a) 4.4 m/s (b) 7.7 m/s (c) 11.7 m/s

Effective Plastic Strain 1.5 **2.0**

Figure 19. Final failure patterns of NSC bottom side subjected to impact force in different impact velocity.

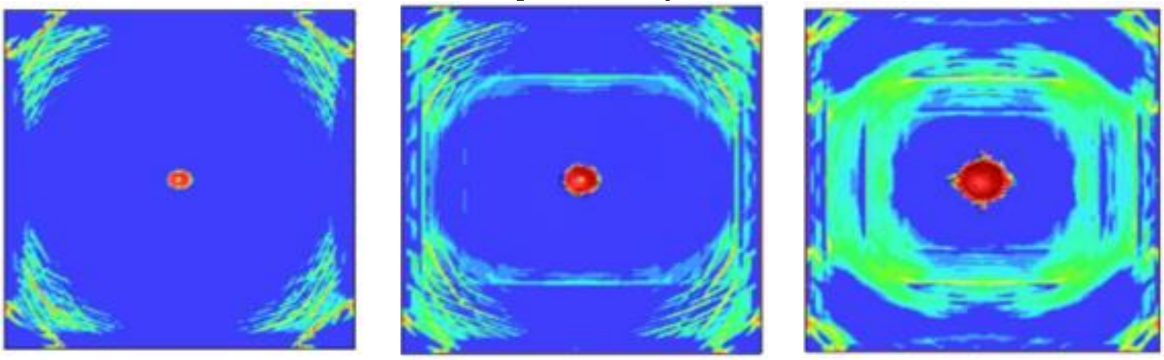

(a) 4.4 m/s (b) 7.7 m/s (c) 11.7 m/s

Effective Plastic Strain 1.5 **2.0**

Figure 20. Final failure patterns of UHPC top side subjected to impact force in different impact velocity.

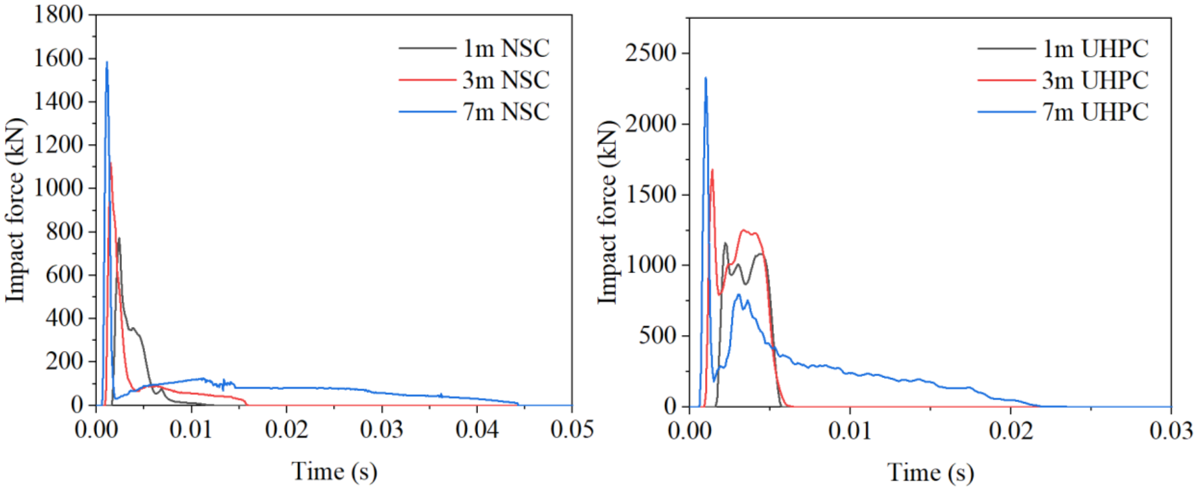

(a) NSC (b) UHPC

Figure 21. Impact force for NSC and UHPC in different impact velocity.

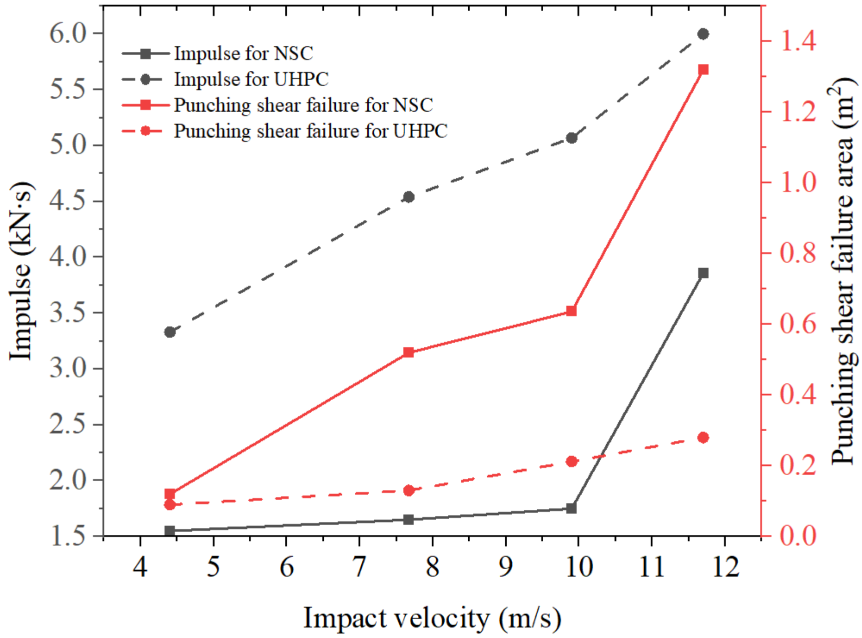

Figure 22. Impulse and punching shear failure area for both NSC and UHPC with different impact velocity.

5.3 Impact mass

The influence of impact mass was studied by changing the weight of punch in 100 kg, 300 kg, and 500 kg as well as 700 kg. Fire-exposed time remained 2 hrs and the impact velocity was set as 9.9 m/s@5 m. Figure 23 reveals the final failure patterns of slabs on the bottom side subjected to impact force in different impact mass for both the NSC and UHPC slabs. The increase in impact mass resulted in a worse localised damage of the RC slab. It was evdient that more and more circumferential and radial cracks were developed after increasing the impact mass. The punching shear failures for NSC in 100 kg, 300 kg and 700 kg were 4.45 times, 3.96 times and 3.55 times larger than UHPC (see Figure 25). Furthermore, the decline in impact force was caused by the reduction in impact mass (see Figure 24). The peak impact forces for NSC for 100 kg, 300 kg and 700 kg were 1129 kN, 1261 kN and 1328 kN, respectively. The peak impact forces for UHPC for 100 kg, 300 kg and 700 kg were 1660 kN, 1930 kN and 2040 kN, respectively. Moreover, the impulse for NSC in 100 kg, 300 kg and 700 kg were 1.1 kN·s, 1.7 kN·s, 1.9 kN·s, which were 1.1 times, 0.6 times, 0.3 times of UHPC, respectively (see Figure 25).

(1)

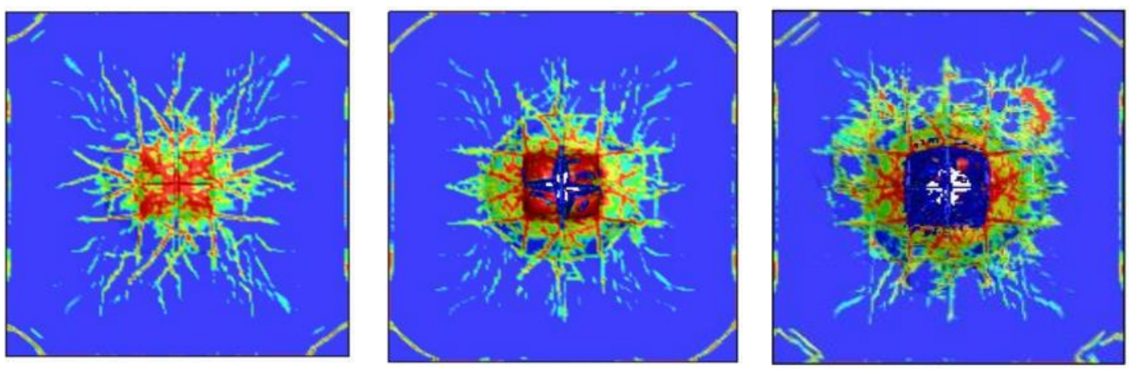

(a) 100 kg (b) 300 kg (c) 700 kg

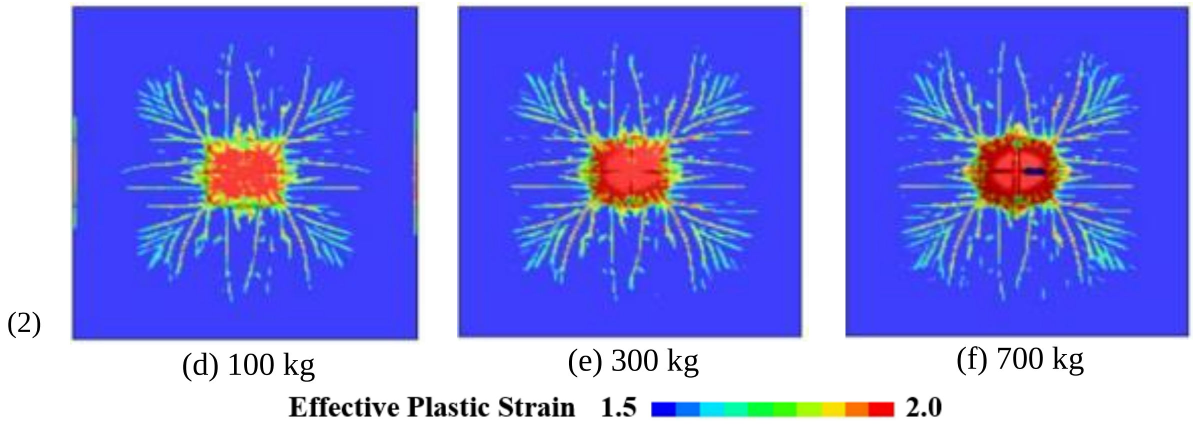

Figure 23. Final failure patterns of slabs on bottom side subjected to impact force in different impact mass. (1) NSC (2) UHPC

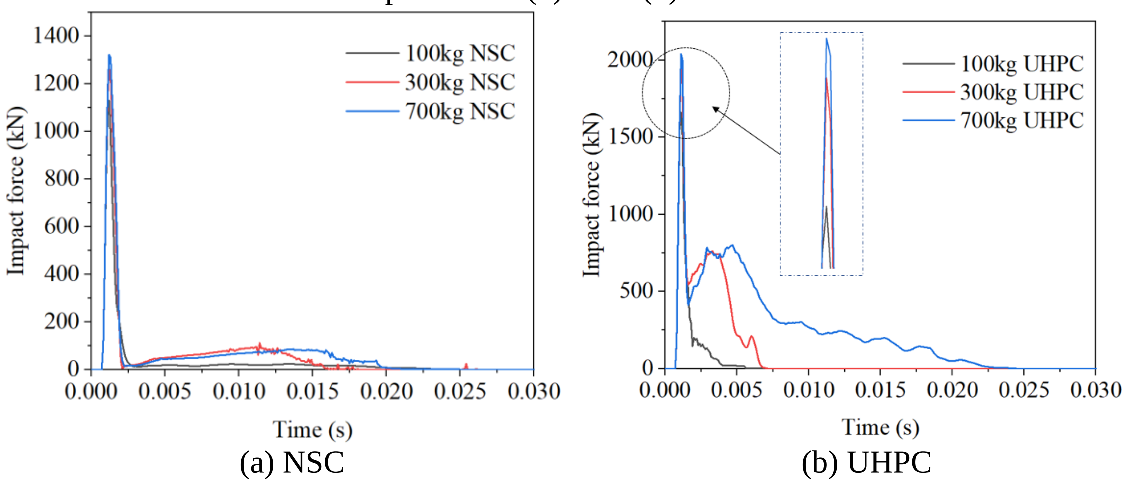

Figure 24. Impact force in different impact mass.

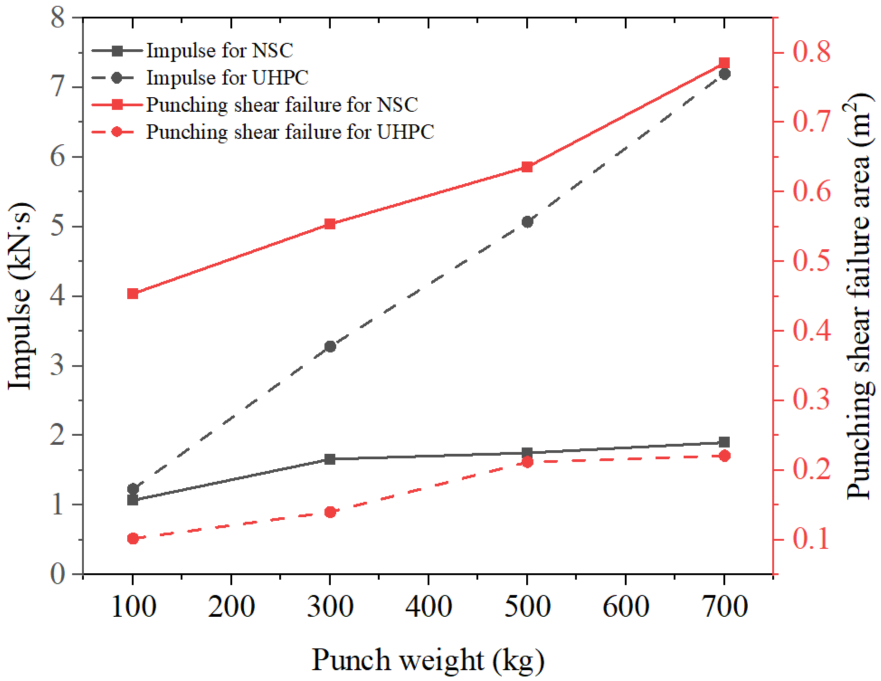

Figure 25. Impulse and punching shear failure area for both NSC and UHPC with different punch weight.

6 Conclusion

Post-fire impact resistance of the UHPC and NSC slabs is studied with refined finite element modelling. The KCC model has been modified including the strength surfaces, λ-η relationships, damage accumulation parameters, strain rate curve and equation of state for both NSC and UHPC after exposure to elevated temperature. The modified KCC model has been used for validation regarding a post-fire RC structure to impact loading experiment. The following inferences are made in light of this study:

- Failure strength parameters and state of equation should be modified after exposure to elevated temperature for UHPC material.
- The UHPC slabs exhibited a higher impact resistance than the NSC slabs after exposure to fire. Although the UHPC slabs experienced higher peak impact force and impulse, they exhibited reduced punching shear failure and lower mid-point deflection.
- The development and severity to localized damage were highly affected by fire-exposed time. The longer exposure time to fire, the larger damage area was. The punching shear failures in NSC were 2.5 times, 3.4 times, 3.0 times and 1.2 times larger than UHPC after exposure to fire at 1, 2, 3 and 4 hrs, respectively. After exposure to 4 hrs ISO fire, both the UHPC and NSC slabs demonstrated accelerated strength deterioration.
- With the increase in impact velocity, the punching shear damage area and peak impact force increased. The punching shear failures of the NSC slabs were 1.3 times, 4.0 times, 3.0 times, and 4.7 times more than the UHPC slabs at 4.4 m/s, 7.7 m/s, and 9.9 m/s as well as 11.7 m/s impact, respectively.
- The reduction in impact mass led to less cracks and damage area as well as lower impact force. The punching shear failures for the NSC slabs in 100 kg, 300 kg, and 500 kg as well as 700 kg were 4.5 times, 4.0 times, 3.0 times and 3.6 times larger than the UHPC slab after exposure to the same fire load.

Reference:

1. Gyu-Yong, K., K. Young-Sun, and L. Tae-Gyu, *Mechanical properties of high-strength concrete subjected to high temperature by stressed test.* Transactions of Nonferrous metals society of China, 2009. **19**: p. s128-s133.
2. Khaliq, W., *Mechanical and physical response of recycled aggregates high-strength concrete at elevated temperatures.* Fire safety journal, 2018. **96**: p. 203-214.
3. Phan, L.T. and N.J. Carino, *Review of mechanical properties of HSC at elevated temperature.* Journal of Materials in Civil Engineering, 1998. **10**(1): p. 58-65.
4. Kumar, V., M.A. Iqbal, and A. Mittal, *Experimental investigation of prestressed and reinforced concrete plates under falling weight impactor.* Thin-Walled Structures, 2018. **126**: p. 106-116.
5. Wu, C., D. Oehlers, M. Rebentrost, J. Leach, and A. Whittaker, *Blast testing of ultra-high performance fibre and FRP-retrofitted concrete slabs.* Engineering structures, 2009. **31**(9): p. 2060-2069.
6. Li, J., C. Wu, and H. Hao, *An experimental and numerical study of reinforced ultra-high performance concrete slabs under blast loads.* Materials & Design, 2015. **82**: p. 64-76.
7. Xu, J., et al., *Behaviour of ultra high performance fibre reinforced concrete columns subjected to blast loading.* Engineering Structures, 2016. **118**: p. 97-107.
8. Chan, S.Y., G.-f. Peng, and J.K. Chan, *Comparison between high strength concrete and normal strength concrete subjected to high temperature.* Materials and Structures, 1996. **29**(10): p. 616-619.
9. Xiao, J., Q. Xie, and W. Xie, *Study on high-performance concrete at high temperatures in China (2004–2016)-An updated overview.* Fire safety journal, 2018. **95**: p. 11-24.
10. Abrams, M.S., *Compressive strength of concrete at temperatures to 1600F.* Special Publication, 1971. **25**: p. 33-58.
11. Wang, W., D. Zhang, F. Lu, S.-C. Wang, and F. Tang, *Experimental study on scaling the explosion resistance of a one-way square reinforced concrete slab under a close-in blast loading.* International Journal of Impact Engineering, 2012. **49**: p. 158-164.
12. Fujikake, K., T. Senga, N. Ueda, T. Ohno, and M. Katagiri, *Study on impact response of reactive powder concrete beam and its analytical model.* Journal of advanced concrete technology, 2006. **4**(1): p. 99-108.
13. Yoo, D.-Y. and N. Banthia, *Mechanical and structural behaviors of ultra-high-performance fiber-reinforced concrete subjected to impact and blast.* Construction and Building Materials, 2017. **149**: p. 416-431.
14. Wei, J., J. Li, and C. Wu, *An experimental and numerical study of reinforced conventional concrete and ultra-high performance concrete columns under lateral impact loads.* Engineering Structures, 2019. **201**: p. 109822.
15. Wang, W., C. Wu, J. Li, Z. Liu, and Y. Lv, *Behavior of ultra-high performance fiber-reinforced concrete (UHPFRC) filled steel tubular members under lateral impact loading.* International Journal of Impact Engineering, 2019. **132**: p. 103314.
16. Kahanji, C., F. Ali, and A. Nadjai, *Explosive spalling of ultra-high performance fibre reinforced concrete beams under fire.* Journal of Structural Fire Engineering, 2016.
17. Citek, D., M. Rydval, S. Rehacek, and J. Kolísko. *Material properties of ultra-high performance concrete in extreme conditions*. in *Key Engineering Materials*. 2016. Trans Tech Publ.
18. Xiong, M.-X. and J.R. Liew, *Spalling behavior and residual resistance of fibre reinforced Ultra-High performance concrete after exposure to high temperatures.* Materiales de Construcción, 2015. **65**(320): p. e071-e071.

19. Xiong, M.-X. and J.R. Liew, *Mechanical behaviour of ultra-high strength concrete at elevated temperatures and fire resistance of ultra-high strength concrete filled steel tubes.* Materials & Design, 2016. **104**: p. 414-427.
20. Zheng, W., B. Luo, and Y. Wang, *Compressive and tensile properties of reactive powder concrete with steel fibres at elevated temperatures.* Construction and Building Materials, 2013. **41**: p. 844-851.
21. Felicetti, R., P.G. Gambarova, M.N. Sora, and G.A. Khoury. *Mechanical behaviour of HPC and UHPC in direct tension at high temperature and after cooling*. in *Fifth RILEM symposium on fibre-reinforced concretes, N*. 2000.
22. Sanchayan, S. and S.J. Foster, *High temperature behaviour of hybrid steel–PVA fibre reinforced reactive powder concrete.* Materials and Structures, 2016. **49**(3): p. 769-782.
23. Zhang, D., K.H. Tan, A. Dasari, and Y. Weng, *Effect of natural fibers on thermal spalling resistance of ultra-high performance concrete.* Cement and Concrete Composites, 2020. **109**: p. 103512.
24. Chen, L., Q. Fang, X. Jiang, Z. Ruan, and J. Hong, *Combined effects of high temperature and high strain rate on normal weight concrete.* International Journal of Impact Engineering, 2015. **86**: p. 40-56.
25. Yu, X., L. Chen, Q. Fang, Z. Ruan, J. Hong, and H. Xiang, *A concrete constitutive model considering coupled effects of high temperature and high strain rate.* International Journal of Impact Engineering, 2017. **101**: p. 66-77.
26. Su, H., J. Xu, and W. Ren, *Experimental study on the dynamic compressive mechanical properties of concrete at elevated temperature.* Materials & Design (1980-2015), 2014. **56**: p. 579-588.
27. Li, Z., J. Xu, and E. Bai, *Static and dynamic mechanical properties of concrete after high temperature exposure.* Materials Science and Engineering: A, 2012. **544**: p. 27-32.
28. Huo, J., Y. He, L. Xiao, and B. Chen, *Experimental study on dynamic behaviours of concrete after exposure to high temperatures up to 700 C.* Materials and structures, 2013. **46**(1): p. 255-265.
29. Zhai, C., L. Chen, Q. Fang, W. Chen, and X. Jiang, *Experimental study of strain rate effects on normal weight concrete after exposure to elevated temperature.* Materials and Structures, 2017. **50**(1): p. 1-11.
30. Liang, X., C. Wu, Y. Yang, and Z. Li, *Experimental study on ultra-high performance concrete with high fire resistance under simultaneous effect of elevated temperature and impact loading.* Cement and Concrete Composites, 2019. **98**: p. 29-38.
31. Jin, L., J. Bai, R. Zhang, L. Li, and X. Du, *Effect of elevated temperature on thelow-velocity impact performances of reinforced concrete slabs.* International Journal of Impact Engineering, 2021. **149**: p. 103797.
32. Ožbolt, J., D. Ruta, and B. İrhan, *Impact analysis of thermally pre-damaged reinforced concrete slabs: verification of the 3D FE model.* International Journal of Impact Engineering, 2019. **133**: p. 103343.
33. Jin, L., Y. Lan, R. Zhang, and X. Du, *Impact performances of RC beams at/after elevated temperature: A meso-scale study.* Engineering Failure Analysis, 2019. **105**: p. 196-214.
34. Ožbolt, J., L. Lacković, and D. Ruta, *Impact analysis of thermally pre-damaged reinforced concrete frames.* Materials, 2020. **13**(23): p. 5349.
35. Ruta, D., *Numerical and experimental study of concrete structures exposed to impact and fire.* 2018.

36. Chen, W., Z. Guo, T. Zhang, H. Zou, and J. Gu, *Near-field blast test on reactive powder concrete-filled steel tubular columns after exposure to fire*. International Journal of Protective Structures, 2016. **7**(2): p. 193-212.
37. Xu, Z., J. Li, C. Wu, and P. Wu, *Experimental investigation of triaxial strength of ultra-high performance concrete after exposure to elevated temperature.* Construction and Building Materials, 2021, Accepted.
38. Malvar, L.J., J.E. Crawford, J.W. Wesevich, and D. Simons, *A plasticity concrete material model for DYNA3D.* International journal of impact engineering, 1997. **19**(9-10): p. 847-873.
39. Borrvall, T. and W. Riedel. *The RHT concrete model in LS-DYNA*. in *Proceedings of The 8th European LS-DYNA user conference*. 2011.
40. Wu, Y., J.E. Crawford, and J.M. Magallanes. *Performance of LS-DYNA concrete constitutive models*. in *12th International LS-DYNA users conference*. 2012.
41. Lin, X., *Numerical simulation of blast responses of ultra-high performance fibre reinforced concrete panels with strain-rate effect.* Construction and Building Materials, 2018. **176**: p. 371-382.
42. Joy, S. and R. Moxley, *Material characterization, WSMR-5 3/4-inch concrete.* Report to the Defense Special Weapons Agency, 1993.
43. Malvar, L.J., J.E. Crawford, and K.B. Morrill, *K&C concrete material model release III-automated generation of material model input.* Karagozian and Case Structural Engineers, 2000. **Technical Report 650 TR-99-24.3**.
44. Hammoud, R., A. Yahia, and R. Boukhili, *Triaxial compressive strength of concrete subjected to high temperatures.* Journal of materials in civil engineering, 2014. **26**(4): p. 705-712.
45. Ren, G., H. Wu, Q. Fang, J. Liu, and Z. Gong, *Triaxial compressive behavior of UHPCC and applications in the projectile impact analyses.* Construction and Building Materials, 2016. **113**: p. 1-14.
46. Xu, Z., J. Li, H. Qian, and C. Wu, *Blast resistance of hybrid steel and polypropylene fibre reinforced ultra-high performance concrete after exposure to elevated temperatures.* Composite Structures, 2022: p. 115771.
47. Naus, D.J., *The Effect of Elevated Temperature on Concrete Materials and Structures-a Literature Review.* 2006.
48. Khoury, G., *Compressive strength of concrete at high temperatures: a reassessment.* Magazine of concrete Research, 1992. **44**(161): p. 291-309.
49. Xu, Z., J. Li, P. Wu, and C. Wu, *Experimental investigation of triaxial strength of ultra-high performance concrete after exposure to elevated temperature.* Construction and Building Materials, 2021. **295**: p. 123689.
50. Chang, Y.-F., Y.-H. Chen, M.-S. Sheu, and G.C. Yao, *Residual stress–strain relationship for concrete after exposure to high temperatures.* Cement and concrete research, 2006. **36**(10): p. 1999-2005.
51. Reinhardt, H.W., H.A. Cornelissen, and D.A. Hordijk, *Tensile tests and failure analysis of concrete.* Journal of structural engineering, 1986. **112**(11): p. 2462-2477.
52. Li, Y. and D. Zhang, *Effect of lateral restraint and inclusion of polypropylene and steel fibers on spalling behavior, pore pressure, and thermal stress in ultra-high-performance concrete (UHPC) at elevated temperature.* Construction and Building Materials, 2021. **271**: p. 121879.
53. Li, H. and G. Liu, *Tensile properties of hybrid fiber-reinforced reactive powder concrete after exposure to elevated temperatures.* International Journal of Concrete Structures and Materials, 2016. **10**(1): p. 29-37.

54. Wu, Y. and J.E. Crawford, *Numerical modeling of concrete using a partially associative plasticity model.* Journal of Engineering Mechanics, 2015. **141**(12): p. 04015051.
55. Béton, C.E.-I.d., *CEB-FIP model code 1990: Design code*. 1993: Thomas Telford Publishing.
56. CEB, *CEB-FIP MODEL CODE 90*. 1990, Paris: Federation Internationale de la Precontrainte.
57. Committee, A. *Building code requirements for structural concrete (ACI 318-08) and commentary*. 2008. American Concrete Institute.
58. Graybeal, B.A., *Compressive behavior of ultra-high-performance fiber-reinforced concrete.* ACI materials journal, 2007. **104**(2): p. 146.
59. Liang, X., C. Wu, Y. Su, Z. Chen, and Z. Li, *Development of ultra-high performance concrete with high fire resistance.* Construction and Building Materials, 2018. **179**: p. 400-412.
60. du Beton, C.E.-I. *Fire Design of Concrete Structures in Accordance with CEB/FIP Model Code 90*. in *Lausanne, Switzerland*. 1991.
61. *EN, 1992-1-2: design of concrete structures. Part 1-2: general rules-structural fire design*. in *Eurocode 2*. 2002. Brussels, Belgium: European Committee for Standardization.
62. Neel, C., *Compaction and spall of UHPC concrete under shock conditions.* Journal of Dynamic Behavior of Materials, 2018. **4**(4): p. 505-528.
63. Erzar, B., C. Pontiroli, and E. Buzaud, *Shock characterization of an ultra-high strength concrete.* The European Physical Journal Special Topics, 2016. **225**(2): p. 355-361.
64. Gao, L., *Reasearch on high pressure equation of RPC.* Guangzhou: Guangzhou University, 2011: p. 42e8.
65. ISO, I., *834: Fire resistance tests-elements of building construction.* International Organization for Standardization, Geneva, Switzerland, 1999.
66. Mohan, J., *Fire endurance of concrete slabs with dolomite aggregates*. 1981, Carleton University.
67. Banerjee, D.K., *A Review of Models for Heat Transfer in Steel and Concrete Members During Fire.* Journal of Research of the National Institute of Standards and Technology, 2021. **126**: p. 1-33.
68. Tao, Z., X.-Q. Wang, and B. Uy, *Stress-strain curves of structural and reinforcing steels after exposure to elevated temperatures.* Journal of Materials in Civil Engineering, 2013. **25**(9): p. 1306-1316.
69. Béton, C.E.-I.d., *Concrete structures under impact and impulsive loading: Synthesis report*. 1988: Comite euro-international du beton.
70. Qi, C., A. Remennikov, L.-Z. Pei, S. Yang, Z.-H. Yu, and T.D. Ngo, *Impact and close-in blast response of auxetic honeycomb-cored sandwich panels: experimental tests and numerical simulations.* Composite structures, 2017. **180**: p. 161-178.
71. Forni, D., B. Chiaia, and E. Cadoni, *Blast effects on steel columns under fire conditions.* Journal of Constructional Steel Research, 2017. **136**: p. 1-10.